

# **Status of High latitude precipitation estimates from observations and reanalyses**

**Ali Behrangi\***

Jet Propulsion Laboratory, California Institute of Technology, Pasadena, California, USA

**Matthew Christensen**

Science and Technology Facilities Council, Rutherford Appleton Laboratory, Didcot, UK  
Atmospheric, Oceanic and Planetary Physics, University of Oxford, Oxford, UK

**Mark Richardson, Matthew Lebsack, Graeme Stephens,**

Jet Propulsion Laboratory, California Institute of Technology, Pasadena, California, USA

**George J. Huffman, David Bolvin**

NASA Goddard Space Flight Center, Greenbelt, Maryland, USA

**Robert F. Adler**

Earth System Science Interdisciplinary Center, University of Maryland, College Park,  
Maryland, USA

**Alex Gardner, Bjorn Lambrigtsen, Eric Fetzer**

Jet Propulsion Laboratory, California Institute of Technology, Pasadena, California, USA

**Submitted to:** *J. of Geophysical Research*

*\*Corresponding author:*

Ali Behrangi,

Jet Propulsion Laboratory, California Institute of Technology.

4800 Oak Grove Drive , MS 233-304, Pasadena, CA 91109, USA.

E-mail: Ali.Behrangi@jpl.nasa.gov; Tel: +1 818-393-8657

Key points:

- 1- ERA- Interim and MERRA agree closely with CloudSat precipitation over high-latitude oceans.
- 2- Over Antarctica total snowfall from GPCP and CloudSat is almost identical: about 178 mm/yr.
- 3- GPCP likely overestimates snowfall over Eurasia.

## Abstract

2 An intercomparison of high-latitude precipitation characteristics from observation-  
3 based and reanalysis products is performed. In particular the precipitation products  
4 from CloudSat provide an independent assessment to other widely used products, these  
5 being the observationally-based GPCP, GPCC and CMAP products and the ERA-Interim,  
6 MERRA and NCEP-DOE R2 reanalyses. Seasonal and annual total precipitation in both  
7 hemispheres poleward of 55° latitude is considered in all products, and CloudSat is used  
8 to assess intensity and frequency of precipitation occurrence by phase, defined as rain,  
9 snow or mixed phase. Furthermore, an independent estimate of snow accumulation  
10 during the cold season was calculated from the Gravity Recovery and Climate  
11 Experiment (GRACE). The intercomparison is performed for the 2007-2010 period  
12 when CloudSat was fully operational. It is found that ERA- Interim and MERRA are  
13 broadly similar, agreeing more closely with CloudSat over oceans. ERA-Interim also  
14 agrees well with CloudSat estimates of snowfall over Antarctica where total snowfall  
15 from GPCP and CloudSat is almost identical. A number of disagreements on regional or  
16 seasonal scales are identified: CMAP reports much lower ocean precipitation relative to  
17 other products, NCEP-DOE R2 reports much higher summer precipitation over northern  
18 hemisphere land, GPCP reports much higher snowfall over Eurasia, and CloudSat  
19 overestimates precipitation over Greenland, likely due to mischaracterization of rain and  
20 mixed-phase precipitation. These outliers are likely unrealistic for these specific regions  
21 and time periods. These estimates from observations and reanalyses provide useful  
22 insights for diagnostic assessment of precipitation products in high latitudes, quantifying

23 the current uncertainties, improving the products, and establishing a benchmark for  
24 assessment of climate models.

25

26 **1. Introduction**

27 Precipitation characteristics are expected to change in a warming climate [Trenberth  
28 2003; Stephens et al., 2008]. Accurate quantification of the amount and distribution of  
29 precipitation is critical to understanding the current state of Earth's climate and water  
30 and energy budget [Stephens et al., 2012; Trenberth et al., 2007; Rodell et al., 2015;  
31 L'Ecuyer et al., 2015], and how the hydrological cycle responds to the energy  
32 imbalances that force climate change [Andrews et al., 2009]. Changes in the amount,  
33 frequency, and intensity of precipitation can significantly impact regional hydrologic  
34 processes and may have severe impacts on socioeconomic sectors and agricultural  
35 productivity.

36

37 High-latitude regions respond more strongly to anthropogenic climate change than  
38 other regions according to surface temperature observations and climate model  
39 simulations [Serreze and Francis, 2006; Solomon et al., 2007], and an intensification of  
40 high-latitude precipitation is also projected by climate models [Lau et al., 2013].  
41 Reported changes in high-latitude hydrology have been inferred from changes in snow  
42 cover, mountain glacier area, permafrost extent and lake area [Smith et al., 2005; Alley et  
43 al. 2007], and increasing freshwater discharge [Yang et al., 2002; Dyurgerov and Carter,  
44 2004; McClelland et al., 2006]. Reduced uncertainty in precipitation estimates is  
45 required to fully contextualize these changes, understand physical processes, and

46 reliably detect and quantify possible changes in the high-latitude hydrological cycle [Ye  
47 et al., 2014].

48

49 Climate models are known to contain large biases in precipitation [Stephens et al., 2010]  
50 and observational precipitation products contain large uncertainties [Behrangi et al.,  
51 2012] particularly where ground measurements are sparse, such as over the oceans and  
52 high-latitude regions [Adler et al., 2012]. It is therefore essential to characterize and  
53 utilize other observation sources to quantify high-latitude precipitation. This is  
54 especially important as the number of precipitation gauges at northern high latitudes  
55 has sharply decreased since 1990 [Serreze et al., 2005] and only a handful of gauges are  
56 operating in Antarctica. Furthermore, existing gauges often face large biases caused by a  
57 number of factors such as wind-induced undercatch [Goodison et al., 1998], particularly  
58 for snow, where correction factors can lead to uncertainties of order 100% [Yang et al.,  
59 2005; Fuchs et al., 2001].

60

61 Given the importance and challenge of quantifying high-latitude precipitation, the  
62 present study investigates high-latitude precipitation from products that are often used  
63 in climate analysis and assessments of climate models. Furthermore, newly emerged  
64 capabilities for quantification of high-latitude precipitation with the CloudSat Cloud  
65 Profiling Radar (CPR)[Stephens et al., 2008] and the Gravity Recovery and Climate  
66 Experiment (GRACE)[Tapley et al., 2004] are exploited to provide independent  
67 precipitation or accumulation estimates.

68

69 CloudSat provides direct observations of snow and light rainfall at high latitudes with  
70 unprecedented signal sensitivity (e.g., minimum detectable signal of  $\sim$ 28 dBZ) but, it  
71 suffers from occasional signal saturation which we ameliorate here by referring to the  
72 Advanced Microwave Scanning Radiometer-Earth Observing System (AMSR-E). CloudSat  
73 provides a rain product that is optimized for use over the oceans where no gauges are  
74 available, and a snow product that is designed to work over both land and ocean, and  
75 which is not vulnerable to the large uncertainties introduced by gauge undercatch of  
76 snow in windy conditions. Another instrument that has shown highly useful for  
77 measuring total snow accumulation [Landerer et al., 2010; Swenson, 2010] is NASA's  
78 Gravity Recovery And Climate Experiment (GRACE) satellite mission. GRACE provides  
79 monthly observations of changes in the Earth's gravity field and is well suited for  
80 measuring changes in continental-scale water storage. To our knowledge this is the first  
81 time that global high latitude precipitation is assessed using such various datasets.

82

83 Detailed information about the products, instruments and methods are provided in  
84 Section 2. Section 3 reports and discusses the results of the intercomparison split by  
85 region before Section 4 concludes.

86

## 87 **2. Data resources and methods**

88 Current precipitation products may be considered as belonging to one of four groups:  
89 gauge-only, satellite-only, satellite and gauge, and reanalysis. Each product was  
90 remapped onto a common  $2.5^\circ \times 2.5^\circ$  lat-lon grid to match the lowest-resolution dataset,  
91 avoiding issues with downscaling and ensuring sufficient CloudSat retrievals within each

92 grid cell. We remapped the products using linear spatial interpolation. While there are  
93 numerous interpolation schemes available (e.g., Kriging, Linear, Natural Neighbor,  
94 Nearest Neighbor, Polynomial Regression), we use linear interpolation as it makes very  
95 little difference on the gridded quantity averages. These methods were applied to  
96 CloudSat precipitation rates and found that the choice of the method resulted in a  
97 maximum difference of 0.005% compared to the linear method. Intercomparison is  
98 conducted for the period 2007 to 2010, during which both CloudSat and AMSR-E were  
99 almost fully functional.

100

## 101 **2.1 Gauge product**

### 102 **2.1.1 GPCC**

103 The Global Precipitation Climatology Centre (GPCC) was established in 1989 at  
104 Deutscher Wetterdienst under the World Meteorological Organization (WMO) as the in  
105 situ component of the Global Precipitation Climatology Project (GPCP) of the Global  
106 Energy and Water Exchanges (GEWEX) project. GPCC integrates data from various  
107 networks, organizations, and additional precipitation data through bilateral contacts and  
108 with the support of WMO to its database [Schneider et al., 2014] and thus employs more  
109 gauges compared to other popular gauge products. However, in many regions --  
110 especially at high latitudes-- gauges are sparse or non-existent. For example, only a  
111 handful of gauges are operating over entire Antarctic and Greenland (Fig. 1). Therefore,  
112 gauge-based estimates of precipitation in these regions have to rely on interpolation of  
113 sparse data, reducing the quality of the product there.

114 Before merging the data from different sources, quality control and homogenization of  
115 station metadata are performed, but the product does not include bias correction for  
116 systematic gauge measuring errors. In this study we used GPCC Full Data Reanalysis  
117 Version 7.0 at  $2.5^\circ \times 2.5^\circ$  resolution. Details for construction of gridded precipitation  
118 products and data access are described in Becker et al. (2013) and Schneider et al.  
119 [2014; 2015].

120

## 121 **2.2. Satellite-gauge products**

### 122 **2.2.1 GPCP**

123 GPCP was formed as a community-based analysis of global precipitation under the  
124 auspices of the World Climate Research Program (WCRP) and is being widely used by  
125 the research community. GPCP is a merged product using data from gauges over land,  
126 and from spaceborne sensors over both land and ocean including Special Sensor  
127 Microwave Imager (SSMI), Special Sensor Microwave Imager/Sounder (SSMIS), and  
128 geostationary and polar orbiting infrared imagers and sounders. Gauge-based estimates  
129 are adjusted for gauge undercatch using climatological factors. In the high latitudes  
130 (starting at  $\sim 40^\circ$ ), precipitation (including snow) rate is obtained using a regression  
131 relationship between historical collocated rain gauge measurements (adjusted for wind  
132 loss, including relation to snow) and a few cloud-related parameters (e.g., cloud-top  
133 pressure, fractional cloud cover, and cloud-layer relative humidity; Susskind et al.  
134 [1997]). The cloud parameters are retrieved from Television Infrared Observation  
135 Satellite (TIROS) Operational Vertical Sounder (TOVS) and Atmospheric Infrared  
136 Sounder (AIRS).

137 The latest version of the monthly  $2.5^\circ \times 2.5^\circ$  resolution GPCP product (version 2.2;  
138 Huffman and Bolvin, [2012]) available from Goddard Earth Sciences Data and  
139 Information Services Center (GES DISC) is used. Detailed description of the product can  
140 be found in [Adler et al., 2003; Huffman et al., 2009; Huffman and Bolvin, 2012].

141

## 142 **2.2.2 CMAP**

143 The Climate Prediction Center (CPC) Merged Analysis of Precipitation (CMAP) product  
144 [Xie and Arkin, 1997] is also widely used. CMAP provides gridded global monthly  
145 estimate of precipitation at monthly  $2.5^\circ \times 2.5^\circ$  resolution using many of the same  
146 datasets as GPCP. It also uses precipitation data from Microwave Sounding Units (MSUs).  
147 However, the merging of the individual data sources is different from GPCP. Unlike GPCP  
148 it does not use AIRS/TOVS in high latitudes and makes no undercatch adjustment for  
149 gauge measurements. Over land, the blended analysis is controlled by gauge  
150 observations which capture snowfall, but over ocean the satellite estimates (IR and  
151 PMW) implicitly include snowfall as they only estimate total precipitation and snow  
152 remains to be difficult to retrieve. The product was obtained from the NOAA's Earth  
153 System Laboratory via: <http://www.esrl.noaa.gov/psd/data/gridded/data.cmap.html>.  
154 Unlike GPCP, CMAP does not adjust gauge-based estimates for assumed undercatch.

155

## 156 **2.3. Satellite-only products**

### 157 **2.3.1. CloudSat**

158 The 94-GHz nadir-looking CPR on CloudSat provides unprecedented sensitivity to  
159 retrieve snowfall and light rain. The CPR footprint is  $\sim 1.7$  km along track and  $\sim 1.4$  km

160 cross track. CloudSat precipitation data have been invaluable in advancing cold-region  
161 and high-latitude precipitation analysis [Behrangi et al., 2012; 2014a,b; Palerme et al,  
162 2014].

163

164 Three CloudSat products are used here: 2C-PRECIP-COLUMN R04 (henceforth “2c-  
165 column”; Haynes et al. 2009), 2C-RAIN-PROFILE R04 (henceforth “2c-rain”)[Lebsack and  
166 L’Ecuyer, 2011] and 2C-SNOW-PROFILE (henceforth “2c-snow”)[Wood et al., 2013 and  
167 2014] along with the CloudSat auxiliary AMSR-E product CS\_AMSRE-AUX (henceforth  
168 “AMSR-E”) generated by CloudSat team. All data are available at:  
169 <http://www.cloudsat.cira.colostate.edu>.

170 The 2c-column product provides precipitation occurrence through flags representing  
171 the phase (rain, snow or mixed) and likelihood of precipitation (certain, probable,  
172 possible). The 2c-rain product then calculates rain rate when the flag is certain for rain  
173 or mixed phase, while the 2c-snow product calculates snow also in snow possible cases  
174 provided that the estimated melted fraction is under 0.1. For consistency we restrict our  
175 analysis to “certain” for all phases. Where the flag is rain certain, the corresponding  
176 intensity is extracted from 2c-rain, for snow certain the intensity is taken from 2c-snow,  
177 and for mixed phase certain the mean value from 2c-snow and 2c-rain is used if both are  
178 nonzero, otherwise the single nonzero value from 2c-snow or 2c-rain is used. This  
179 occurs in few cases due to temperature or melted-fraction thresholds in the retrieval  
180 algorithms.

181

182 In intense rain the radar signal is saturated and the CloudSat algorithm provides a lower  
183 limit on the rain intensity, although some adjustments can be made to provide better  
184 estimates of heavy precipitation [Stephens et al., 2010; Matrosov, 2014]. Here we choose  
185 to make no adjustment and select the largest value out of this lower limit and the  
186 coincident AMSR-E from CS\_AMSRE-AUX. In the Southern Hemisphere poleward of 55°  
187 latitude (SH55), 0.4% of rain events result in saturation, and in the Northern  
188 Hemisphere poleward of 55° (NH55) 0.2% are saturated. Thus, while there is a potential  
189 underestimate of precipitation rates in the most intense events, the size of this  
190 underestimate should be limited by the rarity of these events and the inclusion of AMSR-  
191 E retrievals.

192

193 Similarly, the exclusion of possible or probable precipitation events may lead to an  
194 underestimate, although analysis of the 2c-snow product suggests that this is also small.  
195 Non-certain events tend to be of low intensity and in the case of the 2c-snow product,  
196 including non-certain snow events would only increase the mean snowfall rate in the  
197 SH55 region by +2.9% and in the NH55 region by +4.5%.

198

199 There are further issues to consider regarding the CloudSat rain rate retrieval algorithm.  
200 Firstly, it uses ocean reflectance properties in its path integrated attenuation approach  
201 [Haynes et al., 2009]. Over land the surface reflectivity properties are not as well known,  
202 resulting in uncertainty in the rain rate retrievals. The magnitude of any potential bias  
203 has not yet been quantified. Secondly, when the surface topography is rough the CPR  
204 may receive backscatter from ice or land surfaces at high altitudes, which it

205 misinterprets as being very intense near surface rain. The 2c-snow algorithm uses  
206 vertical reflectivity continuity tests to eliminate this scenario, but these tests have not  
207 been applied to the 2c-rain product to date. The above issues affect only the rain rates  
208 retrieved over land, and not the frequency of occurrence or snow rates. A relevant  
209 concern for all of the CloudSat retrievals is that it does not fully sample the diurnal cycle  
210 with overpasses occurring near 1:31 a.m. and 1:31 p.m. local time. We are unable to  
211 correct for this sampling issue and it remains an unquantified source of uncertainty.  
212 However, as shown in Behrangi et al. [2012] the effect is likely small over ocean.

213

### 214 **2.3.2. GRACE**

215 The Gravity Recovery and Climate Experiment (GRACE) data are used to calculate  
216 precipitation accumulation during the winter season over land. GRACE is a twin satellite  
217 mission that has measured range-rate variations between the two satellites using  
218 microwave interferometry since 2002. Gravity changes due to mass redistribution by  
219 solid-earth processes and hydrology perturb the GRACE orbit, allowing retrieval of mass  
220 variations with high accuracy [Tapley et al., 2004]. GRACE has been used extensively to  
221 study changes in terrestrial water stores (snow, ice, surface water, soil moisture, and  
222 groundwater [Niu et al., 2007; Swenson and Wahr, 2007; Swenson et al., 2006; Swenson  
223 et al., 2010; Landerer et al., 2010].

224

225 During winter, almost all land poleward of 55° latitude experiences near surface  
226 temperature below -2°C, and hence much of the precipitation falls as snow.  
227 Evapotranspiration and runoff are relatively small in winter [Serreze et al., 2003;

228 Lammers et al., 2001], such that, after accounting for solid earth processes, the gravity  
229 anomaly measured by GRACE over high latitude regions at this time of year is primarily  
230 due to the accumulated snowfall. A GRACE-based estimate of winter precipitation  
231 accumulation is unique in that: (i) it is based on a completely independent technique  
232 (gravimetry versus radiometry) with no need for empirical parameterizations, ground-  
233 based calibration, or correction for gauge undercatch, (ii) it captures accumulated  
234 precipitation so does not miss precipitation occurring between satellite overpasses, and  
235 (iii) during wintertime, other satellites and ground measurements face the highest  
236 uncertainty. Furthermore, the measurement noise of GRACE is smallest in high latitudes  
237 because of GRACE's high density of orbits there.

238

239 Precipitation accumulation is calculated from GRACE Terrestrial Water Storage Anomaly  
240 (TWSA) based on mass conservation [Dingman, 2008]. If  $t_1$  is accumulation start-time  
241 (e.g., early winter) and  $t_2$  is the accumulation end-time (e.g., late winter) for domain D,  
242 the water storage change between time  $t_1$  and  $t_2$  can be calculated as

$$243 S(t_2) - S(t_1) = \Delta P - \Delta ET - \Delta Q \quad (\text{Eq. 1})$$

244 Where  $S$ ,  $P$ ,  $ET$ ,  $Q$ , represent water storage, precipitation, evapotranspiration, and  
245 discharge for domain D, respectively and  $\Delta$  represents the net change between  $t_1$  and  $t_2$ .  
246  $\Delta P$  is the accumulated precipitation during winter.

247

248 Over the Greenland and Antarctic ice sheets, the use of GRACE to estimate the  
249 accumulated snowfall is complicated by ice divergence (continual export of mass from

250 the interior to the oceans via ice flow)[Rignot et al., 2011]. Therefore, the present study  
251 does not include these regions in the analysis.

252

253 Monthly  $1^{\circ} \times 1^{\circ}$  gridded GRACE total water storage anomalies are obtained from the  
254 latest release (RL 5) from Center for Space Research at University of Texas, Austin (CSR )  
255 with corrections applied [Landerer and Swenson, 2012; Swenson and Wahr, 2006],  
256 available at <http://gracetellus.jpl.nasa.gov/>. Sakumura et al. [2014] showed that using  
257 an ensemble average of the gravity field solutions from CSR and two other processing  
258 centers can reduce noise. However, differences between the three products are small  
259 and fall within the error bounds of the GRACE solution itself. Evapotranspiration and  
260 runoff are obtained from GLDAS Noah Land Surface Model L4 monthly  $0.25 \times 0.25$   
261 degree Version 2.0 (GLDAS\_NOAH025\_M) product [Rodell et al., 2004], available from  
262 NASA Goddard Earth Sciences (GES) Data and Information Services Center (DISC). The  
263 calculations are performed at  $1^{\circ} \times 1^{\circ}$  resolution and the results are mapped to the  
264 common  $2.5^{\circ} \times 2.5^{\circ}$  resolution used for comparison

265

## 266 **2.4. Reanalysis products**

### 267 **2.4.1. ERA-interim**

268 ERA-interim [Dee et al., 2011; Simmons, 2014] is the latest European Center for  
269 Medium-Range Weather Forecasting (ECMWF) global atmospheric reanalysis. ERA-  
270 interim relies on a 4D-VAR (rather than 3D-Var as in ERA-40) system which uses  
271 observations within 12-hour windows to initialize forecast simulations. This study uses

272 daily precipitation obtained from <http://apps.ecmwf.int/datasets/> at  $1.5^\circ \times 1.5^\circ$  spatial  
273 resolution.

274

#### 275 **2.4.2. MERRA**

276 The Modern Era Retrospective-Analysis for Research and Applications (MERRA)  
277 [Rienecker et al., 2011; Bosilovich et al., 2011] uses the Goddard Earth Observing System  
278 Data Assimilation System version 5 (GEOS-5; Rienecker et al., [2011]) to assimilate  
279 observations (e.g., radiance data) for the retrospective analyses. In the present study  
280 precipitation is obtained from the latest version of the MERRA product (V 5.2) available  
281 at GES DISC with resolution of  $2/3^\circ$  longitude by  $1/2^\circ$  latitude.

282

#### 283 **2.4.3. NCEP-DOE R2**

284 The National Centers for Environmental Prediction-Department of Energy Reanalysis 2  
285 (NCEP-DOE R2) product [Kanamitsu et al., 2002] uses a global data assimilation system  
286 and numerical weather prediction model to produce atmospheric analyses using  
287 historical data and also to produce analyses of the current atmospheric state from 1979  
288 to the present. The Reanalysis-2 product fixed errors and updated parameterizations of  
289 physical processes that hampered earlier versions. This product has 17 vertical pressure  
290 levels globally gridded at T62 spatial resolution ( $\sim 1.875^\circ \times 1.875^\circ$ ) four times daily. Data  
291 is provided by the NOAA-ESRL Physical Sciences Division, Boulder Colorado from their  
292 web site at <http://www.esrl.noaa.gov/psd/>.

293

#### 294 **2.5 Calculation method for precipitation characteristics**

295 **2.5.1 Development of CloudSat gridded products**

296 CloudSat data are transferred onto a  $2.5^\circ \times 2.5^\circ$  grid, and the mean monthly intensity  
297 climatology is estimated by dividing the sum of all precipitation intensities for the month  
298 and grid cell by the total number of valid measurements determined as the cases in  
299 which 2c-column status\_flag < 10. CloudSat is also used to provide maps of the frequency  
300 of rain occurrence, and the total number of certain precipitation retrievals is divided by  
301 the total number of valid retrievals within a grid cell. Reported precipitation frequency  
302 depends on the spatial scale, in this case reported values are precipitation frequency at  
303 the natural scale of the CPR footprint.

304

305 In each case separate maps were produced for rain, mixed-phase precipitation and  
306 snow, and these were summed to obtain total precipitation rate or frequency.

307

308 **2.5.2 Calculation of regional and hemispheric precipitation rates**

309 Total precipitation rates from each product were calculated for a number of regions  
310 including the northern hemisphere north of  $55^\circ\text{N}$  (NH55), southern hemisphere south of  
311  $55^\circ\text{S}$  (SH55). As CloudSat only fully covers grid cells in the latitude band  $80^\circ\text{N-S}$ , area-  
312 mean intensities for hemispheric averages are only reported for the  $55^\circ\text{-}80^\circ$  latitude  
313 bands.

314

315 In addition, the hemispheric averages were split into land and ocean and separate  
316 estimates were made for the Greenland and Antarctic ice sheets. For each product these  
317 estimates were made by multiplying the total precipitation in each grid cell by the

318 relevant area-weighted land or ocean fraction determined from the 0.125° ERA-Interim  
319 land-sea mask.

320

321 **3. Results**

322 **3.1. Northern hemisphere (NH)**

323 **3.1.1. CloudSat precipitation frequency and intensity**

324 Figure 2 shows maps of annual and seasonal rain, mixed-phase, snow, and total  
325 precipitation frequencies calculated using four years of CloudSat observations in NH55.

326 The first row displays the annual frequencies and the remaining rows are for  
327 precipitation frequencies for each of the four seasons: winter (DJF), spring (MAM),  
328 summer (JJA), and fall (OND). The map shows that snow is the most frequent land  
329 precipitation type in all seasons except summer, while rain and mixed-phase  
330 precipitation are more frequent over the southern part of the Atlantic Ocean, Gulf of  
331 Alaska, and nearby coastal areas where daily surface temperature typically remains  
332 above 0 °C. Boreal summer precipitation mainly occurs as rainfall except in Greenland,  
333 where, due to its high elevation, snowfall remains most frequent. However, rainfall and  
334 mixed-phase precipitation also occur over southern coastal regions of Greenland.

335 Precipitation is most frequent over the Atlantic Ocean and Gulf of Alaska across all four  
336 seasons, occurring 10-30% of the time with a summer minimum and winter maximum  
337 across almost the entire region north of 55°N. As discussed in Behrangi et al. [2012],  
338 precipitation frequency is sensitive to spatial scale so the values in Figure 2 should be  
339 interpreted cautiously.

340

341 Figure 3 shows seasonal precipitation rates from CloudSat stratified by precipitation  
342 phase. Patterns in intensity are similar to those in occurrence frequency in Figure 2,  
343 except that rainfall events are consistently more intense than snow thus contributing  
344 more to the total precipitation. The intense seasonal precipitation over the Atlantic  
345 Ocean is mainly from rainfall and mixed phase precipitation, with the largest  
346 contribution during boreal fall and winter when the Atlantic storm tracks are most  
347 active.

348 **3.1.2. NH55 Annual precipitation intensity by region**

349 Figure 4 shows maps of average precipitation rates (mm/day) over NH55 constructed  
350 from various products. GPCC is based on gauge observations so reports no ocean data.  
351 According to CloudSat (Fig 4a), the highest precipitation rates are in the North Atlantic  
352 up to the coast of Greenland and along southern coast of Alaska. This pattern is  
353 qualitatively consistent with the other land-ocean products except for CMAP. GPCC (Fig.  
354 4g) agrees well with CloudSat over land (Fig. 4a), but has smaller precipitation rates  
355 over coastal Greenland and southern Alaska. Furthermore, GPCC has slightly higher  
356 precipitation rates than CloudSat over central Canada and Eurasia. As gauges are not  
357 utilized in the CloudSat precipitation estimate, its overall consistency with GPCC is  
358 remarkable. In northern Eurasia, GPCP (Fig 4b) shows a much higher mean  
359 precipitation rate. GPCP and GPCC apply different correction factors to account for gauge  
360 undercatch (e.g. induced by wind) which could contribute to the observed differences  
361 between the two products. In Section 3.1.5 we present analysis of winter-season  
362 precipitation including GRACE accumulation to support these adjustments. Over the  
363 Atlantic Ocean, GPCP does not show a strong north-south gradient in mean precipitation,

364 while other products show a significant decrease in mean precipitation intensity  
365 poleward of approximately 70°N. GPCP displays higher precipitation intensity north of  
366 70°N than the other products, and a lower intensity south of this band than all except for  
367 CMAP, which is a low outlier over all NH55 ocean regions. CMAP's land precipitation  
368 (Fig. 4c) is more consistent with other products, but remains the lowest. Overall, the  
369 observation-based products agree more over land than over ocean, where surface  
370 observations are non-existent. The reanalyses show less disagreement over the spatial  
371 distribution of ocean precipitation than do the observations, and MERRA and ERA-  
372 Interim are particularly consistent. NCEP-DOE R2 reports higher intensity in the  
373 Atlantic, but reports less total ocean precipitation as this is offset by less precipitation in  
374 the Bay of Alaska, North Sea and off the coast of Greenland. MERRA and ERA-Interim  
375 broadly agree with CloudSat both spatially (e.g., by reproducing the strong precipitation  
376 gradient over the Atlantic ocean from north to south of 70°N) and in terms of total ocean  
377 precipitation.

378 Figure 5 shows the mean and standard deviation of precipitation estimates separately  
379 for reanalysis (MERRA, ERA-interim, NCEP-DOE R2; top row) and observation (GPCP,  
380 CMAP, CloudSat; middle row) products. The bottom row is similar to the middle row, but  
381 excludes CMAP. Average precipitation is similar between observations and reanalyses  
382 over ocean when CMAP is excluded, but observations have higher variance over oceans.  
383 The large standard deviation of the satellite-gauge products over ocean is consistent  
384 with findings of Adler et al. [2012]. Note that as CMAP is the notable outlier in total  
385 ocean precipitation estimates, its removal leads to a smaller standard deviation in the  
386 observational products.

387

388 **3.1.3. NH55 Seasonal precipitation by region**

389 Figure 6 shows precipitation mean intensity maps of each product by season. All  
390 products report a strong seasonal cycle over both land and ocean. The Atlantic Ocean  
391 and the Gulf of Alaska receive much of their precipitation during winter and fall, while  
392 land receives more during summer. The outliers once again are CMAP, which shows  
393 suppressed amplitude of the annual cycle and NCEP-DOE R2, which shows much heavier  
394 summer precipitation over land than any other product.

395

396 As summer precipitation tends to be rain and therefore less sensitive to gauge  
397 correction factors, the gauge products should be more reliable in densely instrumented  
398 regions. For example, Bolvin et al. [2009] compared GPCP with independent gauge  
399 measurements in Finland and found good agreement. This suggests that NCEP-DOE R2  
400 may well be overestimating land precipitation, particularly during summer.

401

402 Despite the general agreement in their seasonal patterns, the products show marked  
403 differences in total amount. Over the Atlantic south of 70°N, CloudSat reports average  
404 precipitation during fall and winter greater than 5 mm/day in many cells, exceeding  
405 CMAP and GPCP, but similar to reanalyses. Furthermore, unlike other products, GPCP  
406 does not show any noticeable precipitation gradient around 70°N over the Atlantic  
407 Ocean in any season. In winter and fall, GPCP shows much higher total precipitation than  
408 the other products over Europe, north-west Asia, and over the Atlantic north of 70°N.  
409 The observed higher estimate by GPCP over Eurasia, compared to the other products, is

410 in agreement with that found by Behrangi et al. [2014a] in which overestimation of  
411 GPCP was also noticed using the net surface water exchange rate estimated from  
412 remote-sensing observation and reanalysis. In the next section, this cold season  
413 discrepancy is investigated in more detail by including GRACE estimates of cold-season  
414 accumulation.

415

#### 416 **3.1.4. Implications of GRACE results for cold-season precipitation**

417 Figure 7 compares winter estimates of snowfall from GRACE (Fig 7g) with the other  
418 products over grids experiencing mean 2m air temperature below -1<sup>o</sup>C across all days in  
419 winter. As described in Section 2.1, GRACE-based estimates of winter precipitation are  
420 calculated from Eq. 1 using corresponding evapotranspiration and runoff values from  
421 GLDAS. Note that it was found that the contributions of evapotranspiration and runoff to  
422 the total precipitation are on average about 10% and 0.4%, respectively. Figure 7  
423 suggests that GRACE-based seasonal accumulation of snowfall is comparable to the  
424 other products, except GPCP which shows much higher total precipitation over parts of  
425 northern Eurasia. This again suggests that GPCP likely overestimates precipitation in  
426 this region, which could be related to overcorrection for gauge undercatch problem in  
427 high latitude and especially during winter [Swenson et al., 2010].

428

429 Figure 8 compares the mean accumulated winter snowfall estimated from different  
430 products, over North Asia (Fig. 8a) and North America (Fig. 8b) regions shown in Figure  
431 7. The range of accumulated winter snowfall estimates is 46 mm to 64 mm (or 91 mm  
432 including GPCP) in North Asia and between 34 mm and 50 mm in North America. The

433 average winter snowfall within the identified zones in North America and North Asia are  
434  $42.6 \pm 4.9 (1\sigma)$  mm and  $53.1 \pm 7.5$  mm (or  $58.1 \pm 14.6$  mm including GPCP), respectively.  
435 The GRACE estimate falls well within the estimated range of winter snowfall in both  
436 regions and is consistent with CloudSat, MERRA, and ERA-Interim estimates.

437

### 438 **3.1.5. Comparison of total precipitation**

439 Figure 9 provides a summary of the 2007-2010 average annual precipitation rate and  
440 spatial statistics calculated for each product over the entire NH55, NH55 oceans, NH55  
441 land, and Greenland. Bar charts (top row) show mean precipitation within region by  
442 products and Taylor diagrams [Taylor, 2001] show the centered spatial correlation and  
443 standard deviation relative to GPCP.

444

445 These figures allow estimation of the range of precipitation estimated by observation  
446 and reanalysis and the identification of key disagreements. Over NH55 the all-product  
447 mean $\pm$ standard deviation is  $561 \pm 88$  mm/yr with a range of 386—622 mm/yr. This large  
448 range is due to lower estimates from CMAP, particularly over the ocean. Excluding CMAP  
449 the products show substantially better agreement with mean $\pm$ standard deviation of  
450  $596 \pm 23$  mm/yr and a range of 572—622 mm/yr. Aside from CMAP, both the  
451 observation and reanalysis products are fairly consistent: the maximum difference  
452 between non-CMAP NH55 products is 8%, which means that observations and  
453 reanalyses combined place a relatively tight bound on total precipitation amount for  
454 assessment of climate models or for the precipitation component of the energy budget  
455 over NH55. However, this agreement between non-CMAP products over NH55 at annual

456 scales hides disagreements in the spatial and temporal distribution. From the regional  
457 Taylor diagrams, it can be seen that CloudSat consistently reports larger spatial  
458 variability and in particular is an outlier over Greenland in terms of both total  
459 precipitation (591 mm/yr versus the 300-469 mm/yr range of other products) and its  
460 spatial distribution. CloudSat reports 311 mm/yr of snow and 280 mm/yr of rain and  
461 mixed phased precipitation over Greenland. While the CloudSat estimate of annual  
462 snowfall agrees with previous estimates of precipitation accumulation over Greenland  
463 ice sheet (~300 mm/yr) using ice core, snow pits, and *in situ* measurements [Bales et al.,  
464 2009; Chen et al., 2011], the intensity of rain and mixed-phase precipitation is likely  
465 overestimated. We think this might be related to misinterpretation of radar backscatter  
466 from the rugged topography, and thus the credibility of CloudSat rain retrievals over  
467 Greenland needs to be further investigated. In particular, future revisions to the 2c-rain  
468 product should include vertical continuity tests to prevent the misidentification of  
469 surface clutter as precipitation.

470 Nonetheless, we identify outliers in total precipitation as those whose precipitation  
471 estimate falls outside of 10 % of the range limits of the other products. From this we  
472 identify CMAP over oceans in all seasons except MAM, CloudSat over Greenland in all  
473 seasons except DJF, NCEP over NH55 land during JJA and GPCP over NH55 land during  
474 DJF. These results are consistent with our previous identification of outliers in Sections  
475 3.1.2 through 3.1.4. The Taylor diagrams in Figure 9 provide quantification of the more  
476 qualitative statements made in Section 3.1.2 based on analysis of the maps.

477

478 **3.2. Southern hemisphere (SH)**

479 **3.2.1. CloudSat Precipitation frequency and Intensity**

480 Figure 10 shows maps of annual and seasonal rain, mixed-phase, snow, and total  
481 precipitation frequencies calculated using CloudSat observations collected between  
482 2007 and 2010. The annual frequencies are shown in the first row, followed by  
483 precipitation frequencies for each of the four seasons: DJF, MAM, JJA, and SON.

484

485 Over the Antarctic continent, nearly all precipitation falls as snow and is most  
486 frequent near the coasts, where its frequency of occurrence can exceed 20% in parts of  
487 the Antarctic Peninsula and near some regions of the East Antarctic Ice Sheet. Away from  
488 the coasts frequency of snowfall occurrence can be as low as 5% over the Antarctic  
489 Plateau where elevation exceeds 2 km. The seasonal cycle of precipitation is weak over  
490 the continent and stronger over the ocean, with precipitation more frequent in austral  
491 summer than winter.

492

493 Over oceans the precipitation frequency is highest over the southern Pacific and Indian  
494 Oceans, where it can exceed 30% during austral fall and winter. In general, the seasonal  
495 variability of precipitation occurrence in SH55 (Fig. 10) is much lower than in NH55 (Fig.  
496 2).

497

498 Figure 11 shows the seasonal distribution of rainfall, mixed-phase precipitation,  
499 snowfall, and total precipitation rate over SH55 as observed by CloudSat. The maps  
500 suggest that the intense precipitation region observed at 55°-60°S is mainly composed of  
501 rainfall and mixed-phased precipitation, except in austral winter, when snowfall

502 contribution is the highest. Nearly all precipitation south of 70°S falls as snow during all  
503 seasons and over both ocean and land.

504

### 505 **3.2.2. SH55 Annual precipitation intensity by region**

506 Figure 12 shows maps of annual average precipitation rates (mm/day) over 2007-2010  
507 from CloudSat, GPCP, CMAP, MERRA, ERA-interim, and NCEP-DOE R2 for SH55. No  
508 precipitation data from GPCC exists over the Antarctic continent due to the very sparse  
509 precipitation gauges. The overall pattern of mean annual precipitation is consistent  
510 among the studied products except for CMAP (Fig. 12c). The CloudSat precipitation map  
511 (Fig. 12a) shows higher agreement with MERRA (Fig. 12d) and ERA-Interim (Fig. 12e)  
512 and less agreement with GPCP.

513

514 Unlike other products, GPCP (Fig. 12b) does not show significant longitudinal variation  
515 in precipitation intensity along the band between 55°-60°S and shows continuous  
516 annual precipitation intensity of greater than 3mm/day in this zone. This is consistent  
517 with previous findings indicating that GPCP overestimates zonally averaged  
518 precipitation rates around 60°S (Behrangi et al. 2014). Figure 12c shows that CMAP  
519 consistently underestimates precipitation rates and has wide areas of missing data over  
520 the ocean south of 60°S (shown in white).

521

522 NCEP-DOE R2 consistently reports higher precipitation intensity than MERRA or ERA-  
523 Interim, with a continuous band of heavier precipitation heading equatorward from the  
524 Antarctic Peninsula that is not seen in ERA-Interim, MERRA or CloudSat. NCEP-DOE R2

525 also reports more intense precipitation on the periphery of Wilkes Land, and  
526 penetrating more deeply into the continent from the Bellingshausen and Amundsen Seas  
527 than is seen in other products. CMAP reports rates of order 1 mm/day inland from the  
528 Ronne Ice Shelf to Queen Maud Land, and some larger precipitation rates at the edge of  
529 Kaiser Wilhelm II Land that are not seen in other products.

530

531 Figure 13 shows mean and standard deviation of precipitation estimates, calculated  
532 separately from reanalyses (MERRA, ERA-interim, NCEP-DOE R2; top row), and  
533 observations (GPCP, CMAP, CloudSat; middle row) over SH55. The bottom row is similar  
534 to the middle row, but excludes CMAP from calculations. Consistent with NH55 (Fig 5),  
535 reanalyses show higher agreement among themselves than with observations, especially  
536 over ocean. Removing CMAP suppresses the spread in observational estimates and leads  
537 to regional patterns that are more similar to reanalyses.

538

### 539 **3.2.4. SH55 Seasonal precipitation intensity by region**

540 Figure 14 shows seasonal distribution maps of precipitation mean intensity for the  
541 products for SH55. All of the products (except CMAP) suggest a seasonal variation that is  
542 not as strong as that observed for NH55 (Fig. 6). The products agree that the Southern  
543 Ocean receives much of its precipitation during austral fall and winter. Figure 14 shows  
544 that the GPCP's continuous zonal band of intense precipitation around 60°S (observed in  
545 Fig. 12) is observed across all four seasons, but is more distinct in austral fall. In  
546 particular, there appears to be a discontinuity in GPCP's reported precipitation  
547 intensities at 60°S that is most obvious in austral summer and fall.

548

549 Over West Antarctica and the Antarctic Peninsula, ERA-Interim is most similar to GPCP  
550 and CloudSat throughout the year while MERRA reports more intense local precipitation  
551 from austral fall through spring. NCEP-DOE R2 consistently shows more widespread  
552 snow and continues to report widespread snow during austral summer over the West  
553 Antarctic coast up to where it meets the Ross Ice Shelf, where other products report  
554 little or none.

555

### 556 **3.2.5. Comparison of total precipitation**

557 Figure 15 is similar to Fig. 9, but is over SH55, SH55 ocean, and SH55 land (Antarctica).  
558 Once again, CMAP is a notable low outlier at 303 mm/yr that is mainly related to  
559 underestimation over ocean. Excluding CMAP the products show mean $\pm$ standard  
560 deviation of  $667 \pm 46$  mm/yr and a range of 611—732 mm/yr. Based on CloudSat data,  
561 precipitation totals are split by phase as follows: snow 50.1%, rain 13.7% and mixed-  
562 phase 36.1%. CloudSat is not an outlier over Antarctica as it is over Greenland, perhaps  
563 because the challenges with retrieval of rainfall are not relevant in Antarctica (see Figure  
564 10).

565

566 Over Antarctica, CloudSat reports 178 mm/yr of snowfall, accounting for approximately  
567 97.5% of total precipitation. We consider this to be consistent with the 171 mm/yr by  
568 Palmerme et al. (2014). The remaining 4 % difference may be explained by different time  
569 periods (2007—2010 here versus August 2006 to April 2011 in Palmerme et al. [2014]),  
570 regional coverage (north of 80 °S here, north of 82 °S in Palmerme et al. [2014]) and

571 potentially choice of land-sea mask. This result is also similar to the  $\sim 170\text{mm/yr}$   
572 estimate by Vaughan et al. [1999] who interpolated between a compilation of in situ  
573 surface accumulation measurements throughout Antarctica.

574

575 Among the reanalyses, ERA-Interim is closest to the observations with 193 mm/yr of  
576 total precipitation, while MERRA and NCEP-DOE R2 report 23-37 % more snowfall. It  
577 has been reported that ERA-Interim does not show temporal discontinuities over  
578 Antarctica and likely presents the most realistic depiction of changes in Antarctic  
579 precipitation over 1989-2009 [Bromwich et al., 2011]. ERA-Interim is also in stronger  
580 agreement with CloudSat estimates in terms of both total precipitation and their spatial  
581 statistics shown in the Taylor diagram.

582

583 Figure 15 implies that CMAP is a consistent outlier over both land and ocean, both in  
584 terms of absolute precipitation and spatial distribution. Meanwhile, over oceans GPCP  
585 displays larger spatial variability than other products, in terms of the centered standard  
586 deviation, which is consistent with the latitudinal discontinuity (see Fig. 12). The  
587 clustering of the reanalyses and CloudSat on the Taylor diagram for SH55 ocean suggests  
588 better agreement between these products in the spatial distribution of precipitation.  
589 Unlike in NH55 where we were able to find evidence suggestive of reasons for outliers  
590 (GPCP gauge correction and CloudSat 2c-rain topography issues), we are not able to  
591 identify clear reasons for the magnitude of this spread. As such, it appears that our best  
592 estimates from observation and reanalysis of SH55 precipitation span a larger range

593 than over NH55, with a maximum difference depending on product choice of 18 %,  
594 versus 8 % in NH55.

595

596 **4. Concluding Remarks**

597 Precipitation estimates from ground observation (GPCC), remote sensing (GPCP, CMAP,  
598 CloudSat, and GRACE), and reanalyses (MERRA, ERA-Interim, and NCEP-DOE R2) are  
599 compared in terms of total annual and seasonal precipitation in high-latitude regions  
600 between 55°-80° latitude. Additionally, CloudSat precipitation products are used to  
601 characterize the frequency of precipitation occurrence and precipitation phase. The  
602 period 2007-2010 was selected as this is when CloudSat provides a complete  
603 observation record. CMAP, GPCP and GPCC utilize gauges over land, CloudSat is very  
604 sensitive to light rain and snowfall, and GRACE enables a fully independent estimation  
605 (i.e. gravimetry versus radiometry) of accumulated cold-season precipitation.

606

607 Overall, a fairly good agreement between CloudSat and GPCP is found in total annual  
608 precipitation across the domains studied, with differences of <10% absolute over NH55-  
609 land-ocean, NH55-ocean, SH55 and SH55-ocean while results are almost identical over  
610 Antarctica. However, these totals mask regional and seasonal differences. For example,  
611 CloudSat reports much heavier total precipitation over Greenland, which is attributed to  
612 surface radar returns over rugged topography being misinterpreted as intense rain.  
613 GPCP reports much heavier winter precipitation over northern Eurasia, which is  
614 attributed to a likely issue with gauge correction factors. GPCP also differs from other  
615 products over the Atlantic Ocean where it does not show a distinct latitudinal gradient in

616 precipitation on either side of 70°N, and over the Southern Ocean where there is a  
617 notable discrepancy in precipitation rates at 60°S. CMAP is a clear outlier over the  
618 oceans, with total precipitation 50% lower than the mean of the other products in NH55  
619 and 30% lower in SH55. Over land it also provides the lowest estimate but is less  
620 extreme as an outlier, likely due to its use of ground gauges for bias correction.

621

622 Among the reanalyses, over NH55 MERRA and ERA-Interim are generally consistent  
623 with each other on large spatial scales while NCEP-DOE R2 reports about 20% more  
624 precipitation over land. The most obvious contributor to this higher estimate is high  
625 accumulation during summer. As this is the warm season when land precipitation is  
626 predominantly rain, undercatch uncertainties are smaller, so products utilizing gauge  
627 networks (e.g., GPCP) are more likely to be reliable. MERRA and ERA-Interim are more  
628 consistent with the gauge estimates, suggesting that NCEP-DOE likely overestimates  
629 land precipitation in NH55, particularly during boreal summer. In SH55, reanalyses are  
630 approximately evenly spread over the range 611–732 mm/yr, with ERA-Interim the  
631 lowest and NCEP-DOE R2 the highest. NCEP-DOE R2 is the furthest from CloudSat over  
632 the ocean (13% higher) and especially over Antarctica (44% higher), whereas ERA-  
633 Interim most closely matches the CloudSat and GPCP observed totals. Considerable  
634 seasonal variation is seen in SH55 precipitation maps, but this is weaker than in NH55.  
635 All products agree that SH55-ocean receives much of its precipitation during austral fall  
636 and winter. Antarctica has a weak seasonal cycle with a minimum in winter. CloudSat  
637 reports that precipitation south of 70°S is almost purely from snowfall across all seasons  
638 over both ocean and land. In general, the CloudSat and re-analysis (MERRA and ERA-

639 Interim) results agree well with each other, both in terms of absolute magnitude and  
640 pattern in most areas and this cross-confirmation increases our confidence in their use.  
641 The merit of reanalysis to produce precipitation fields in middle to high latitudes (e.g.,  
642 Adler et al. [2001]) is likely due to large-scale dynamics and moisture convergence  
643 playing a dominant role in precipitation processes and the success at assimilating  
644 conventional and satellite temperature and moisture soundings.

645

646 We find that some regional discrepancies remain between precipitation products, which  
647 suggest locations where they should be used cautiously. For rain over the oceans and  
648 snow over all surfaces, for which the 2c-rain and 2c-snow algorithms were designed,  
649 GPCP, MERRA and ERA-Interim tend to be consistent with CloudSat totals although the  
650 GPCP spatial distribution of rainfall over the ocean is not in good agreement. Over NH55  
651 land where gauge data is used, MERRA and ERA-Interim also agree better with the  
652 gauge-based products than does NCEP-DOE R2. Over Antarctica, ERA-Interim is in best  
653 agreement with both GPCP and CloudSat.

654

655 Issues of concern raised by this intercomparison are that NCEP-DOE R2 reports much  
656 higher summer precipitation over land in NH55 than all other products, that GPCP  
657 reports excess snowfall over northern Eurasia, and that CMAP consistently reports much  
658 less precipitation over oceans. The quality of CloudSat rain estimation over Greenland  
659 also remains a subject for further investigation.

660

661 Although precipitation estimation at higher latitudes is a major challenge that has not  
662 been fully addressed by the Earth observing community, we show in this paper that  
663 some progress has been achieved. This is indicated by the level of agreement between  
664 products derived from independent data sources. The present comparative analysis  
665 provides useful insights for diagnostic assessment of precipitation products in high  
666 latitudes, quantifying uncertainties among observations and reanalyses, and establishing  
667 a benchmark for assessment of climate models. The recently launched Global  
668 Precipitation Measurement (GPM) mission [Hou et al., 2014] deploys a Ka/Ku band dual  
669 frequency precipitation radar (DPR) and a multichannel passive microwave imager  
670 (GMI) on its Core Observatory, covering 65°S-N. The higher sensitivity of GPM core  
671 instruments to light rain and snowfall, extended coverage (compared to 35°S-N for  
672 TRMM), and improvements in precipitation retrieval methods provide unprecedented  
673 opportunities to take on the challenges of quantifying light rain and falling snow. The W-  
674 band radar on CloudSat has snow detection thresholds more than an order of magnitude  
675 lower than the GPM radars [Skofronick-Jackson et al., 2013], suggesting that CloudSat is  
676 highly complementary to the existing suite of spaceborne sensors, especially over high  
677 latitudes where light precipitation is dominant. The occurrence of a battery anomaly in  
678 April 2011 significantly reduced CloudSat's battery capacity. The issue was mitigated by  
679 reconfiguring the spacecraft's operations to what is referred to as the Daylight-Only  
680 Operations (DO-Op) mode in which CloudSat makes radar measurements for ~56% of  
681 each orbit, while the sensitivity of the radar remains essentially unchanged. Successful  
682 operation of the DO-Op mode since 2011 suggests a mission life with reasonable  
683 likelihood of operations through 2019 (CloudSat Senior review 2015). Further near-

684 future W-band observations are expected with the future launch and operation of the  
685 Earth, Clouds, Aerosols and Radiation Explorer (EarthCARE) mission [Illingworth et al.,  
686 2015].

687

688 It is also hoped that comparative analysis over short periods at high latitudes using  
689 CloudSat such as in this study and soon GPM will enable adjustments or corrections to  
690 the remote sensing and analysis techniques utilized to produce long-term global  
691 analyses such as GPCP. Thus these recent observations will help enable a more accurate  
692 and consistent picture of the long-term precipitation climatology and inter-annual and  
693 inter-decadal variations back through the satellite era.

694

695

696 **Acknowledgments.** Datasets were obtained from various sources: The latest version of  
697 monthly GPCP (V2.2) from Goddard Earth Sciences Data and Information Services  
698 Center (GES DISC), CMAP from NOAA Earth System Laboratory  
699 <http://www.esrl.noaa.gov/psd/data/gridded/data.cmap.html>, GPCC Full Data  
700 Reanalysis Version 7.0 at  $2.5^\circ \times 2.5^\circ$  resolution from  
701 [ftp://ftp.dwd.de/pub/data/gpcc/html/download\\_gate.html](ftp://ftp.dwd.de/pub/data/gpcc/html/download_gate.html), GRACE total water storage  
702 from <http://gracetellus.jpl.nasa.gov/>, Era-Interim daily precipitation from  
703 <http://apps.ecmwf.int/datasets/>, MERRA precipitation (V 5.2) from GES DISC, NCEP  
704 precipitation from NOAA-ESRL at <http://www.esrl.noaa.gov/psd/>, and all CloudSat  
705 products from <http://www.cloudsat.cira.colostate.edu>. Some of the datasets used in  
706 this manuscript is also available through the Arctic Observation and Reanalysis

707 Integrated System (Christensen et al. 2016). Evapotranspiration and runoff are obtained  
708 from GLDAS Noah Land Surface Model L4 monthly 0.25 x 0.25 degree Version 2.0  
709 (GLDAS\_NOAH025\_M) product available from GES DISC. We thank Norm Wood and  
710 Tristan L'Ecuyer at University of Wisconsin-Madison for the discussion about the  
711 CloudSat snow product. The research described in this paper was carried out at the Jet  
712 Propulsion Laboratory, California Institute of Technology, under a contract with the  
713 National Aeronautics and Space Administration. Financial support is also made available  
714 from NASA New Investigator Program (NNH13ZDA001N-NIP) and NASA Energy and  
715 Water Cycle Study (NNH13ZDA001N-NEWS) awards. Government sponsorship is  
716 acknowledged.

## References:

Adler, R. F., C. Kidd, G. Petty, M. Morissey, and H. M. Goodman (2001), Intercomparison of global precipitation products: The third Precipitation Intercomparison Project (PIP-3), *Bulletin of the American Meteorological Society*, 82(7), 1377-1396.

Adler, R. F., G. Gu, and G. J. Huffman (2012), Estimating Climatological Bias Errors for the Global Precipitation Climatology Project (GPCP), *Journal of Applied Meteorology and Climatology*, 51(1), 84-99.

Adler, R. F., G. J. Huffman, A. Chang, R. Ferraro, P. P. Xie, J. Janowiak, B. Rudolf, U. Schneider, S. Curtis, D. Bolvin, A. Gruber, J. Susskind, P. Arkin, and E. Nelkin (2003), The version-2 global precipitation climatology project (GPCP) monthly precipitation analysis (1979-present), *Journal of Hydrometeorology*, 4(6), 1147-1167.

Alley, R., et al. (2007), Summary for policymakers, in Climate Change, The Physical Science Basis, Contribution of W.G. I to the Forth Assessment Report of the IPCC, edited by S. Solomon et al., pp. 1-18, Cambridge Univ. Press, Cambridge, U. K.

Andrews, T., P. M. Forster, and J. M. Gregory (2009), A Surface Energy Perspective on Climate Change, *Journal of Climate*, 22(10), 2557-2570.

Bales, R. C., Q. Guo, D. Shen, J. R. McConnell, G. Du, J. F. Burkhart, V. B. Spikes, E. Hanna, and J. C. D. Cappelen (2009), Annual accumulation for Greenland updated using ice core data developed during 2000–2006 and analysis of daily coastal meteorological data, *Journal of Geophysical Research: Atmospheres*, 114(D6).

Becker, A., P. Finger, A. Meyer-Christoffer, B. Rudolf, K. Schamm, U. Schneider, and M. Ziese (2013), A description of the global land-surface precipitation data products of

the Global Precipitation Climatology Centre with sample applications including centennial (trend) analysis from 1901-present, *Earth Syst. Sci. Data*, 5(1), 71-99.

Behrangi, A., G. Stephens, R. F. Adler, G. J. Huffman, B. Lambrigtsen, and M. Lebsock (2014a), An Update on the Oceanic Precipitation Rate and Its Zonal Distribution in Light of Advanced Observations from Space, *Journal of Climate*, 27(11), 3957-3965.

Behrangi, A., Y. Tian, B. H. Lambrigtsen, and G. L. Stephens (2014b), What does CloudSat reveal about global land precipitation detection by other spaceborne sensors?, *Water Resources Research*, 50, 4893-4905.

Behrangi, A., M. Lebsock, S. Wong, and B. Lambrigtsen (2012), On the quantification of oceanic rainfall using spaceborne sensors, *J. Geophys. Res.*, 117(D20), D20105.

Bolvin, D. T., R. F. Adler, G. J. Huffman, E. J. Nelkin, and J. P. Poutiainen (2009), Comparison of GPCP Monthly and Daily Precipitation Estimates with High-Latitude Gauge Observations, *Journal of Applied Meteorology and Climatology*, 48(9), 1843-1857.

Bosilovich, M. G., F. R. Robertson, and J. Chen (2011), Global Energy and Water Budgets in MERRA, *Journal of Climate*, 24(22), 5721-5739.

Bromwich, D. H., J. P. Nicolas, and A. J. Monaghan (2011), An Assessment of Precipitation Changes over Antarctica and the Southern Ocean since 1989 in Contemporary Global Reanalyses\*, *Journal of Climate*, 24(16), 4189-4209.

Chen, L., O. Johannessen, H. Wang, and A. Ohmura (2011), Accumulation over the Greenland Ice Sheet as represented in reanalysis data, *Advances in Atmospheric Sciences*, 28(5), 1030-1038.

Christensen, M. W., A. Behrangi, T. L'Ecuyer, N. B. Wood, M. D. Lebsack, and G. L. Stephens (2016), Arctic Observation and Reanalysis Integrated System: A New Data Product for Validation and Climate Study, *Bulletin of the American Meteorological Society*, doi: <http://dx.doi.org/10.1175/BAMS-D-14-00273.1>

Dee, D. P., S. M. Uppala, A. J. Simmons, P. Berrisford, P. Poli, S. Kobayashi, U. Andrae, et al. (2011), The ERA-Interim reanalysis: configuration and performance of the data assimilation system, *Q. J. R. Meteorol. Soc.*, 137(656), 553-597.

Dingman, S. L. , 2008: *Physical Hydrology*, 2<sup>nd</sup> ed., Waveland Press, Long Grove, IL, 646pp.

Dyurgerov, M. B., and C. L. Carter (2004), Observational Evidence of Increases in Freshwater Inflow to the Arctic Ocean, *Arctic, Antarctic, and Alpine Research*, 36(1), 117-122.

Fuchs, T., J. Rapp, F. Rubel, and B. Rudolf (2001), Correction of synoptic precipitation observations due to systematic measuring errors with special regard to precipitation phases, *Physics and Chemistry of the Earth, Part B: Hydrology, Oceans and Atmosphere*, 26(9), 689-693.

Goodison, B. E., P. Y. T. Louie, and D. Yang, 1998: WMO solid precipitation measurement intercomparison, Rept. 67, 212 pp., World Meteorological Organization, Geneva.

Haynes, J. M., T. S. L'Ecuyer, G. L. Stephens, S. D. Miller, C. Mitrescu, N. B. Wood, and S. Tanelli (2009), Rainfall retrieval over the ocean with spaceborne W-band radar, *Journal of Geophysical Research: Atmospheres*, 114(D8), D00A22.

Hou, A. Y., R. K. Kakar, S. Neeck, A. A. Azarbarzin, C. D. Kummerow, M. Kojima, R. Oki, K. Nakamura, and T. Iguchi (2014), The Global Precipitation Measurement Mission, *Bulletin of the American Meteorological Society*, 95(5), 701-722.

Huffman, G. J., and D. T. Bolvin (2012), GPCP version 2.2 SG combined precipitation data set documentation. 46 pp. [Available online at [ftp://precip.gsfc.nasa.gov/pub/gpcp-v2.2/doc/V2.2\\_doc.pdf](ftp://precip.gsfc.nasa.gov/pub/gpcp-v2.2/doc/V2.2_doc.pdf).]

Huffman, G. J., R. F. Adler, D. T. Bolvin, and G. Gu (2009), Improving the global precipitation record: GPCP Version 2.1, *Geophys. Res. Lett.*, 36(17), L17808.

Illingworth, A. J., H. W. Barker, A. Beljaars, M. Ceccaldi, H. Chepfer, N. Clerbaux, J. Cole, et al. (2015), The EarthCARE Satellite: The Next Step Forward in Global Measurements of Clouds, Aerosols, Precipitation, and Radiation, *Bulletin of the American Meteorological Society*, 96(8), 1311-1332.

Kanamitsu, M., W. Ebisuzaki, J. Woollen, S.-K. Yang, J. J. Hnilo, M. Fiorino, and G. L. Potter (2002), NCEP-DOE AMIP-II Reanalysis (R-2), *Bulletin of the American Meteorological Society*, 83(11), 1631-1643.

Lammers, R. B., A. I. Shiklomanov, C. J. Vörösmarty, B. M. Fekete, and B. J. Peterson (2001), Assessment of contemporary Arctic river runoff based on observational discharge records, *Journal of Geophys. Research: Atmospheres*, 106(D4), 3321-3334.

Landerer, F. W., and S. C. Swenson (2012), Accuracy of scaled GRACE terrestrial water storage estimates, *Water Resources Research*, 48(4), W04531.

Landerer, F. W., J. O. Dickey, and A. Güntner (2010), Terrestrial water budget of the Eurasian pan-Arctic from GRACE satellite measurements during 2003–2009, *Journal of Geophysical Research: Atmospheres*, 115(D23), D23115.

Lau, W. K. M., H. T. Wu, and K. M. Kim (2013), A canonical response of precipitation characteristics to global warming from CMIP5 models, *Geophys. Res. Lett.*, 40(12), 3163-3169.

Lebsack, M. D., and T. S. L'Ecuyer (2011), The retrieval of warm rain from CloudSat, *J. Geophys. Res.*, 116(D20), D20209.

L'Ecuyer, T. S., H. K. Beaudoin, M. Rodell, W. Olson, B. Lin, S. Kato, C. A. Clayson, E. Wood, et al. (2015), The Observed State of the Energy Budget in the Early 21st Century, *Journal of Climate*.

Matrosov, S. Y. (2014), Intercomparisons of CloudSat and Ground-Based Radar Retrievals of Rain Rate over Land, *Journal of Applied Meteorology and Climatology*, 53(10), 2360-2370.

McClelland, J. W., S. J. Déry, B. J. Peterson, R. M. Holmes, and E. F. Wood (2006), A pan-arctic evaluation of changes in river discharge during the latter half of the 20th century, *Geophys. Res. Lett.*, 33(6), L06715.

Mitrescu, C., T. L'Ecuyer, J. Haynes, S. Miller, and J. Turk (2010), CloudSat Precipitation Profiling Algorithm-Model Description, *Journal of Applied Meteorology and Climatology*, 49(5), 991-1003.

Niu, G.-Y., K.-W. Seo, Z.-L. Yang, C. Wilson, H. Su, J. Chen, and M. Rodell (2007), Retrieving snow mass from GRACE terrestrial water storage change with a land surface model, *Geophys. Res. Lett.*, 34(15), L15704.

Palerme, C., J. E. Kay, C. Genthon, T. L'Ecuyer, N. B. Wood, and C. Claud (2014), How much snow falls on the Antarctic ice sheet?, *The Cryosphere Discuss.*, 8(1), 1279-1304.

Rienecker, M. M., M. J. Suarez, R. Gelaro, R. Todling, J. Bacmeister, E. Liu, M. G. Bosilovich, S. D. et al. (2011), MERRA: NASA's Modern-Era Retrospective Analysis for Research and Applications, *Journal of Climate*, 24(14), 3624-3648.

Rignot, E., J. Mouginot, and B. Scheuchl (2011), Ice Flow of the Antarctic Ice Sheet, *Science*, 333(6048), 1427-1430.

Rodell, M., H. K. Beaudoin, T. S. L'Ecuyer, W. S. Olson, J. S. Famiglietti, P. R. Houser, R. Adler, M. G. Bosilovich, et al. (2015), The Observed State of the Water Cycle in the Early Twenty-First Century, *Journal of Climate*, 28(21), 8289-8318.

Rodell, M., P. R. Houser, U. Jambor, J. Gottschalck, K. Mitchell, C. J. Meng, K. Arsenault, B. Cosgrove, J. Radakovich, M. Bosilovich, J. K. Entin\*, J. P. Walker, D. Lohmann, and D. Toll (2004), The Global Land Data Assimilation System, *Bulletin of the American Meteorological Society*, 85(3), 381-394.

Sakumura, C., S. Bettadpur, and S. Bruinsma (2014), Ensemble prediction and intercomparison analysis of GRACE time-variable gravity field models, *Geophys. Res. Lett.*, 41(5), 1389-1397.

Schneider, Udo; Becker, Andreas; Finger, Peter; Meyer-Christoffer, Anja; Rudolf, Bruno; Ziese, Markus (2015), GPCC Full Data Reanalysis Version 7.0 at 2.5°: Monthly Land-Surface Precipitation from Rain-Gauges built on GTS-based and Historic Data, doi: 10.5676/DWD\_GPCC/FD\_M\_V7\_250

Schneider, U., A. Becker, P. Finger, A. Meyer-Christoffer, M. Ziese, and B. Rudolf (2014), GPCC's new land surface precipitation climatology based on quality-controlled in situ data and its role in quantifying the global water cycle, *Theoretical and Applied Climatology*, 115(1-2), 15-40.

Serreze, M., and J. Francis (2006), The Arctic Amplification Debate, *Climatic Change*, 76(3-4), 241-264.

Simmons, A. J., P. Poli, D. P. Dee, P. Berrisford, H. Hersbach, S. Kobayashi, and C. Peubey (2014), Estimating low-frequency variability and trends in atmospheric temperature using ERA-Interim, *Q. J. R. Meteorol. Soc.*, 140(679), 329-353.

Skofronick-Jackson, G. M., B. T. Johnson, and S. J. Munchak (2013), Detection Thresholds of Falling Snow From Satellite-Borne Active and Passive Sensors, *Geoscience and Remote Sensing, IEEE Transactions on*, 51(7), 4177-4189.

Smith, L. C., Y. Sheng, G. M. MacDonald, and L. D. Hinzman (2005), Disappearing Arctic Lakes, *Science*, 308(5727), 1429.

Solomon, S., et al. (2007), Technical summary, in Climate Change 2007: The Physical Science Basis. Contribution of Working Group I to the Fourth Assessment Report of the Intergovernmental Panel on Climate Change, edited by S. Solomon et al., pp. 20–91, Cambridge Univ. Press, Cambridge, U. K.

Stephens, G. L., J. L. Li, M. Wild, C. A. Clayson, N. Loeb, S. Kato, T. L'Ecuyer, P. W. Stackhouse, M. Lebsack, and T. Andrews (2012), An update on Earth's energy balance in light of the latest global observations, *Nat. Geosci.*, 5(10), 691-696.

Stephens, G. L., T. L'Ecuyer, R. Forbes, A. Gettlemen, J.-C. Golaz, A. Bodas-Salcedo, K. Suzuki, P. Gabriel, and J. Haynes (2010), Dreary state of precipitation in global models, *J. Geophys. Res.*, 115(D24), D24211.

Stephens, G. L., and T. D. Ellis (2008), Controls of Global-Mean Precipitation Increases in Global Warming GCM Experiments, *Journal of Climate*, 21(23), 6141-6155.

Susskind, J., P. Piraino, L. Rokke, L. Iredell, and A. Mehta (1997), Characteristics of the TOVS Pathfinder Path A Dataset, *Bulletin of the American Meteorological Society*, 78(7), 1449-1472.

Swenson, S. (2010), Assessing High-Latitude Winter Precipitation from Global Precipitation Analyses Using GRACE, *Journal of Hydrometeorology*, 11(2), 405-420.

Swenson, S., and J. Wahr (2007), Multi-sensor analysis of water storage variations of the Caspian Sea, *Geophys. Res. Lett.*, 34(16), L16401.

Swenson, S., P. J. F. Yeh, J. Wahr, and J. Famiglietti (2006), A comparison of terrestrial water storage variations from GRACE with in situ measurements from Illinois, *Geophys. Res. Lett.*, 33(16), L16401.

Tapley, B. D., S. Bettadpur, J. C. Ries, P. F. Thompson, and M. M. Watkins (2004), GRACE Measurements of Mass Variability in the Earth System, *Science*, 305(5683), 503-505.

Taylor, K. E. (2001), Summarizing multiple aspects of model performance in a single diagram, *Journal of Geophysical Research: Atmospheres*, 106(D7), 7183-7192.

Trenberth, K. E., L. Smith, T. T. Qian, A. Dai, and J. Fasullo (2007), Estimates of the global water budget and its annual cycle using observational and model data, *Journal of Hydrometeorology*, 8(4), 758-769.

Trenberth, K. E., A. Dai, R. M. Rasmusson, and D. B. Parsons (2003), The Changing Character of Precipitation, *Bulletin of the American Meteorological Society*, 84(9), 1205-1217.

Vaughan, D. G., J. L. Bamber, M. Giovinetto, J. Russell, and A. P. R. Cooper (1999), Reassessment of Net Surface Mass Balance in Antarctica, *Journal of Climate*, 12(4), 933-946.

Wilheit, T., C. D. Kummerow, and R. Ferraro (2003), NASDARainfall algorithms for AMSR-E, *IEEE Trans. Geosci. Remote Sens.*, 41(2), 204-214.

Wood, N. B., T. S. L'Ecuyer, A. J. Heymsfield, G. L. Stephens, D. R. Hudak, and P. Rodriguez (2014), Estimating snow microphysical properties using collocated multisensor observations, *Journal of Geophysical Research: Atmospheres*, 119(14), 8941-8961.

Wood, N. B., T. S. L'Ecuyer, F. L. Bliven, and G. L. Stephens (2013), Characterization of video disdrometer uncertainties and impacts on estimates of snowfall rate and radar reflectivity, *Atmos. Meas. Tech.*, 6(12), 3635-3648.

Xie, P. and P. A. Arkin, 1997: Global Precipitation: A 17-Year Monthly Analysis Based on Gauge Observations, Satellite Estimates, and Numerical Model Outputs. *Bulletin of the American Meteorological Society*, 78, 2539-2558.

Yang, D., D. L. Kane, L. D. Hinzman, X. Zhang, T. Zhang, and H. Ye (2002), Siberian Lena River hydrologic regime and recent change, *Journal of Geophysical Research: Atmospheres*, 107(D23), 4694.

Yang, D., D. Kane, Z. Zhang, D. Legates, and B. Goodison (2005), Bias corrections of long-term (1973–2004) daily precipitation data over the northern regions, *Geophys. Res. Lett.*, 32(19), L19501.

Ye, H., E. J. Fetzer, S. Wong, A. Behrangi, E. T. Olsen, J. Cohen, B. H. Lambrigtsen, and L. Chen (2014), Impact of increased water vapor on precipitation efficiency over northern Eurasia, *Geophys. Res. Lett.*, 41(8), 2014GL059830.

Figure captions:

Figure 1. Number of stations in each  $2.5^{\circ}\times 2.5^{\circ}$  grids used in GPCC. The map is constructed by averaging the number of stations during 2007 to 2010.

Figure 2. Maps of annual and seasonal rain, mixed-phase, snow, and total precipitation frequencies calculated using four years of CloudSat observations poleward of  $55^{\circ}\text{N}$ . The first row displays the annual frequencies and the remaining rows are for precipitation frequencies for each of the four boreal seasons: winter (DJF), spring (MAM), summer (JJA), and fall (OND).

Figure 3. Maps of seasonal precipitation rates from CloudSat in NH for 2007-2010, stratified by precipitation phases. From left to right columns represent mean rainfall, mixed-phase, snowfall, and total precipitation and rows display the four boreal seasons. Seasons are winter (DJF), spring (MAM), summer (JJA), and fall (SON)

Figure 4. Maps of four-year averaged precipitation rates (mm/day) for 2007-2010 constructed from CloudSat, GPCP, CMAP, MERRA, ERA-Interim, NCEP, and GPCC over land and ocean north of latitude  $55^{\circ}$ . White areas represent missing or non-reported data.

Figure 5. Maps of mean and standard deviation of precipitation estimates for 2007-2010, calculated separately for reanalysis (MERRA, ERA-Interim, NCEP) and observation (GPCP, CMAP, CloudSat) products in NH.

Figure 6. Maps of precipitation mean intensity for the studied products (shown in rows) across the four boreal seasons and poleward of  $55^{\circ}\text{N}$ . White areas represent missing or non-reported data. Seasons are winter (DJF), spring (MAM), summer (JJA), and fall (SON).

Figure 7. Comparison of wintertime estimate of snowfall rate from GRACE (Fig 6g) with the other products. Only grids experiencing mean 2m air temperatures below  $-1^{\circ}\text{C}$  across all days in boreal winter are considered for this comparison.

Figure 8. Comparison between 2007-2010 mean accumulated boreal winter snowfall estimated by different products separately over (a) Northern Asia and (b) Northern America. The two regions are identical to those shown in Figure 6.

Figure 9: Precipitation statistics for each product by region. Top row: bar charts show mean precipitation (2007-2010) within region by product, organized as reanalyses (left 3 bars) and observations (right bars). The red solid bar shows the mean  $\pm 1$  standard deviation of the reanalysis product means, the dashed black bar shows the mean  $\pm 1$  standard deviation of the observational series GPCP, CMAP and CloudSat, and the solid black bar is the same excluding CMAP. Bottom row: Taylor diagrams of the same regions, product symbols shown in legend (far right) and the reference (black star) is the mean of

the reanalyses plus the geographically complete observations GPCP and CloudSat. Regions are, from left to right: the entire NH (55-80°N), NH oceans (55-80°N), NH land (55-80°N), and Greenland.

Figure 10. Maps of annual and seasonal rain, snow, and precipitation frequencies from CloudSat observations for 2007-2010. The first row displays the annual frequencies and the remaining rows are for precipitation frequencies for each of the four austral seasons: summer (DJF), fall (MAM), winter (JJA), and spring (OND).

Figure 11. Maps of seasonal precipitation rates from CloudSat for 2007-2010, stratified by precipitation phases. From left to right columns represent mean rainfall, mixed-phase, snowfall, and total precipitation and rows display the four austral seasons.

Figure 12. Maps of 2007-2010 averaged precipitation rates (mm/day) constructed from CloudSat, GPCC, GPCP, CMAP, MERRA, ERA-interim, NCEP, and GLDAS over land and ocean south of latitude 55°. White areas represent missing or non-reported data.

Figure 13. Maps of mean and standard of precipitation estimates, calculated separately for reanalysis (MERRA, ERA-Interim, NCEP; bottom row) and observation (GPCP, CMAP, CloudSat) products in SH for 2007-2010.

Figure 14. Maps of precipitation mean intensity for the studied products (shown in rows) across the four austral seasons in SH for 2007-2010. White areas represent missing or non-reported data.

Figure 15. Similar to Fig. 9 but for Southern Hemisphere 55-80° (SH55). Regions are, from left to right: the entire SH (55-80°S), SH oceans (55-80°S), and SH land (55-80°S)(Antarctica). GPCC has no data over Antarctica and is not shown.

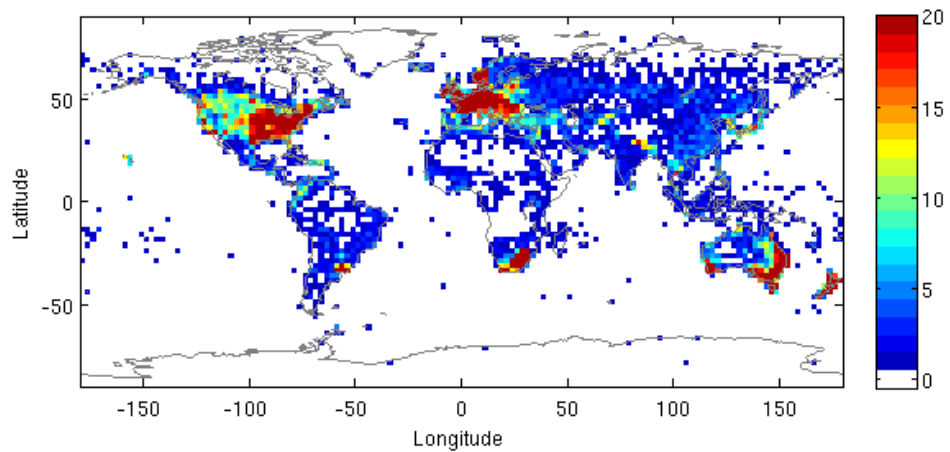


Figure 1. Number of stations in each  $2.5^\circ \times 2.5^\circ$  grids used in GPCC. The map is constructed by averaging the number of stations during 2007 to 2010.

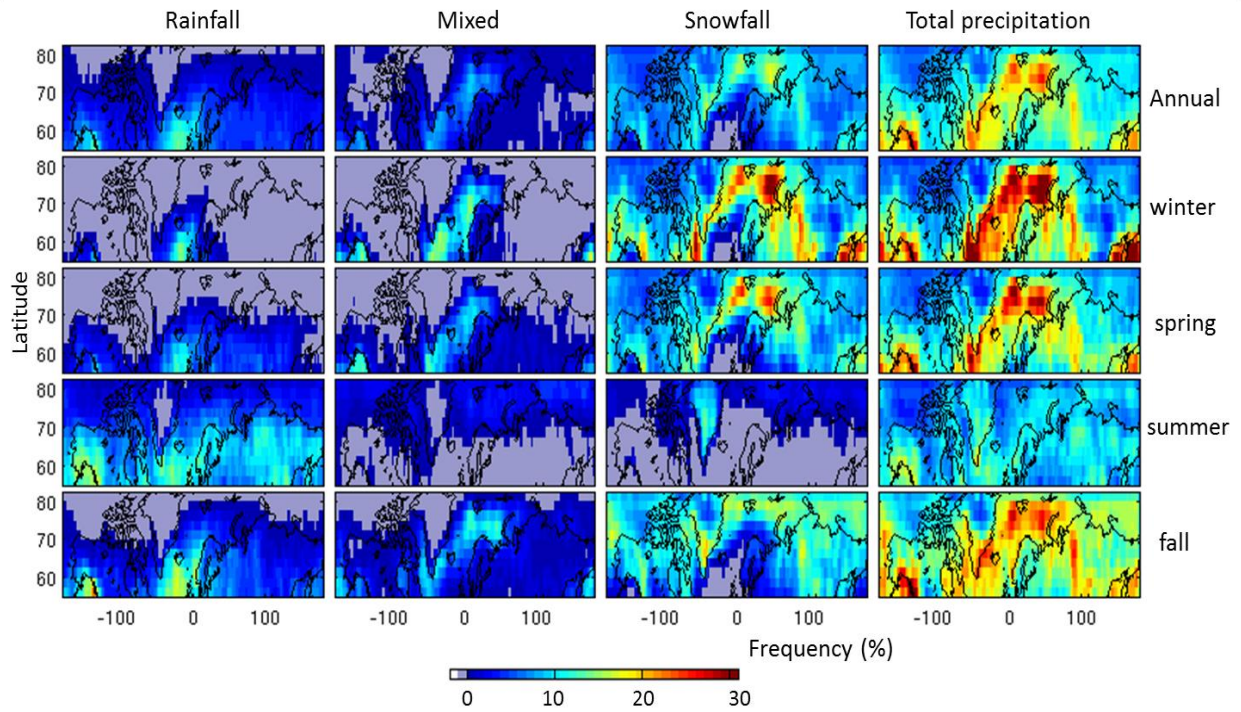


Figure 2. Maps of annual and seasonal rain, mixed-phase, snow, and total precipitation frequencies calculated using four years of CloudSat observations poleward of 55°N. The first row displays the annual frequencies and the remaining rows are for precipitation frequencies for each of the four boreal seasons: winter (DJF), spring (MAM), summer (JJA), and fall (OND).

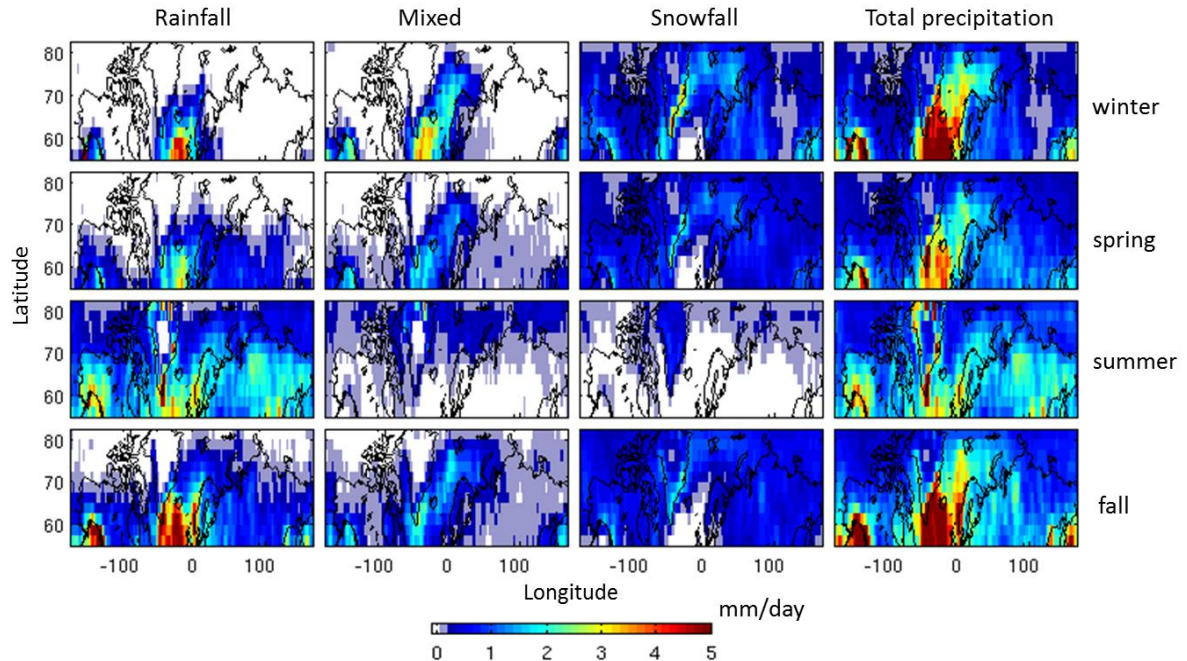


Figure 3. Maps of seasonal precipitation rates from CloudSat in NH for 2007-2010, stratified by precipitation phases. From left to right columns represent mean rainfall, mixed-phase, snowfall, and total precipitation and rows display the four boreal seasons. Seasons are winter (DJF), spring (MAM), summer (JJA), and fall (SON)

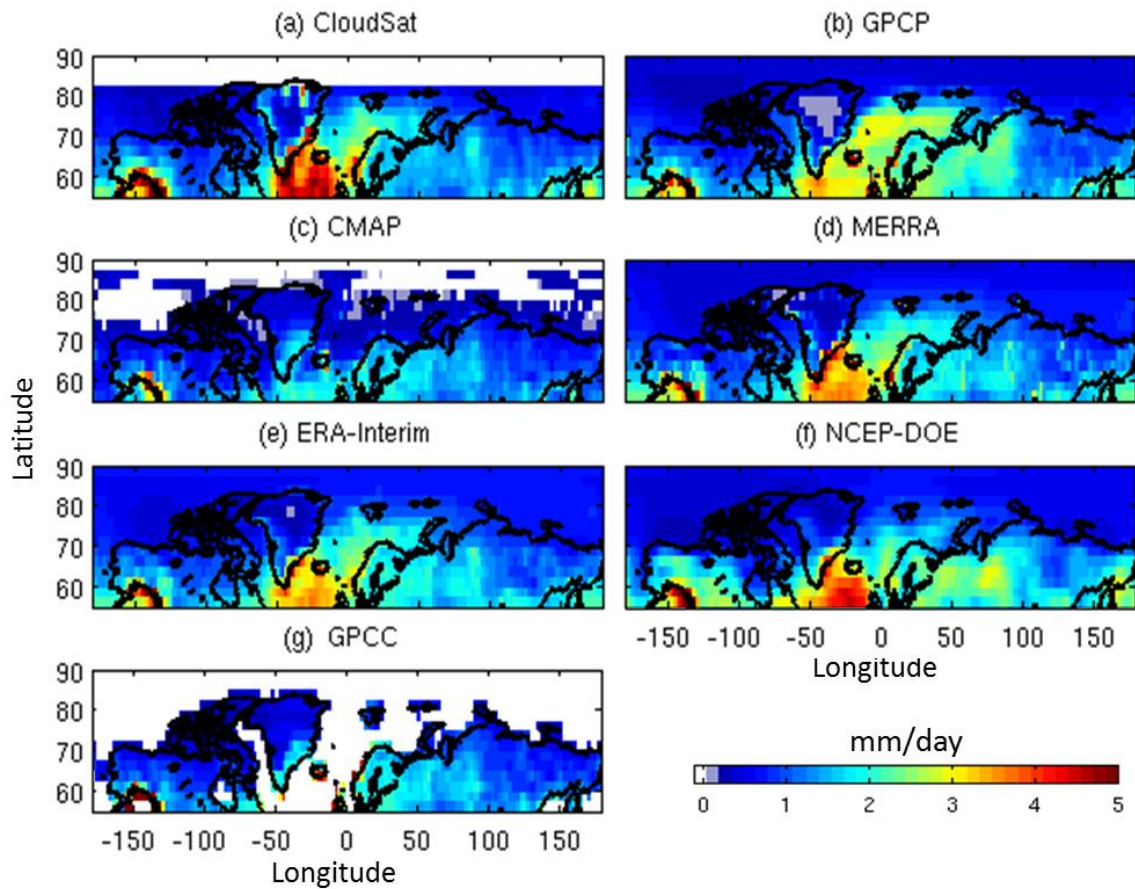


Figure 4. Maps of four-year averaged precipitation rates (mm/day) for 2007-2010 constructed from CloudSat, GPCP, CMAP, MERRA, ERA-Interim, NCEP, and GPCC over land and ocean north of latitude 55°. White areas represent missing or non-reported data.

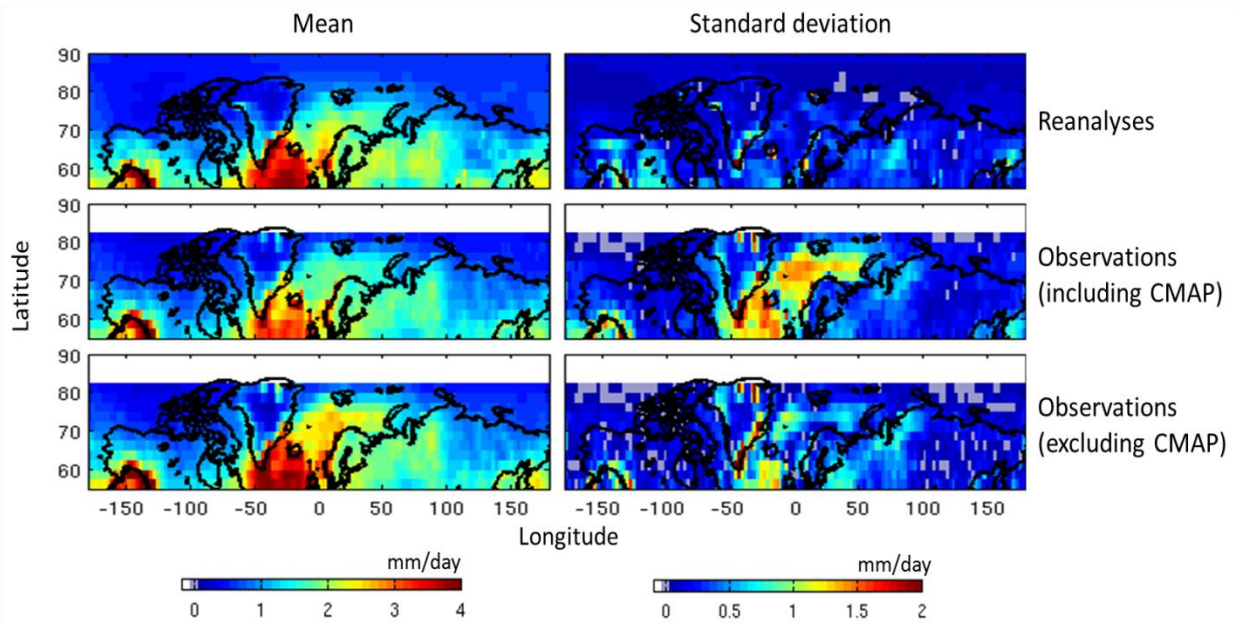


Figure 5. Maps of mean and standard deviation of precipitation estimates for 2007-2010, calculated separately for reanalysis (MERRA, ERA-Interim, NCEP) and observation (GPCP, CMAP, CloudSat) products in NH.

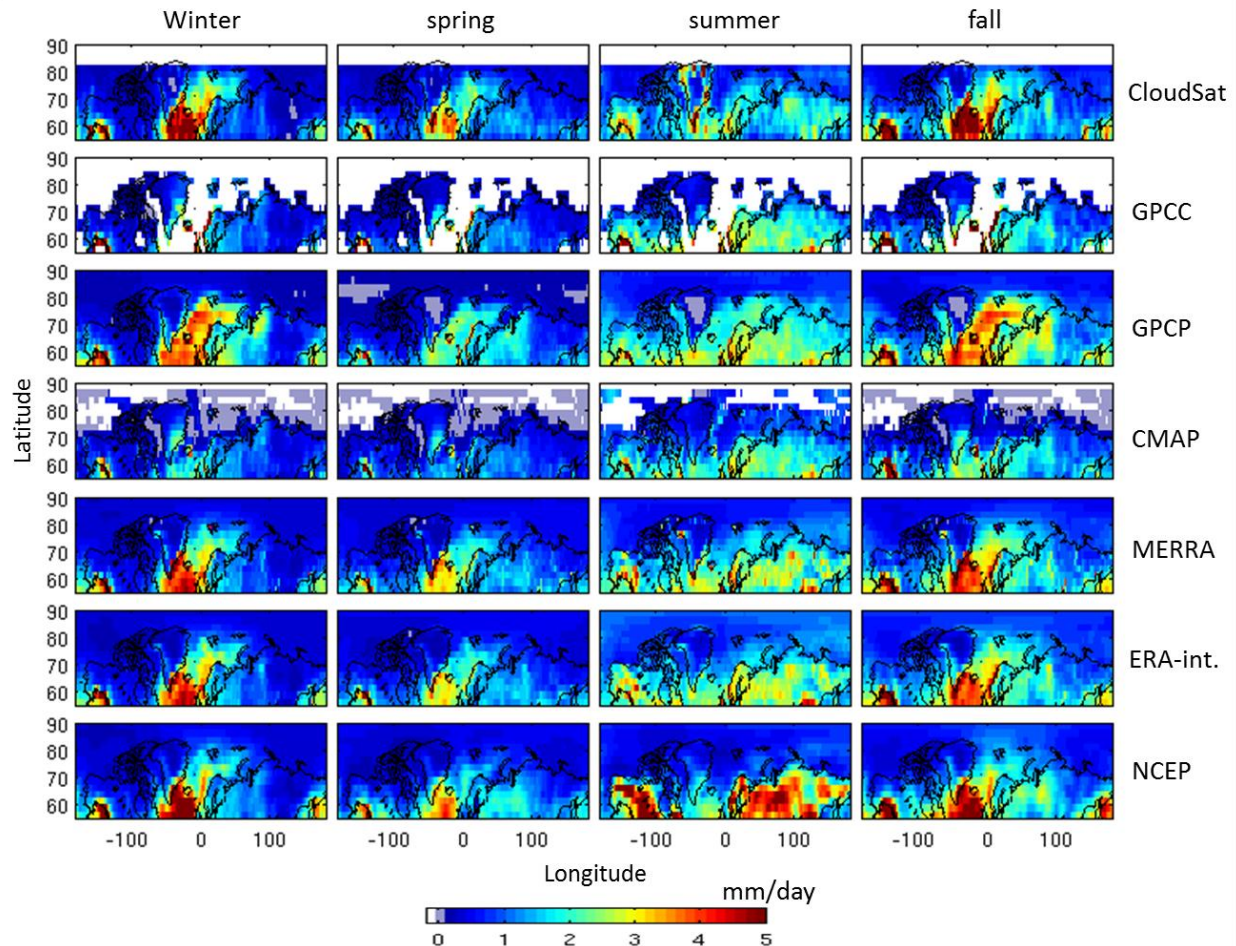


Figure 6. Maps of precipitation mean intensity for the studied products (shown in rows) across the four boreal seasons and poleward of 55°N. White areas represent missing or non-reported data. Seasons are winter (DJF), spring (MAM), summer (JJA), and fall (SON).

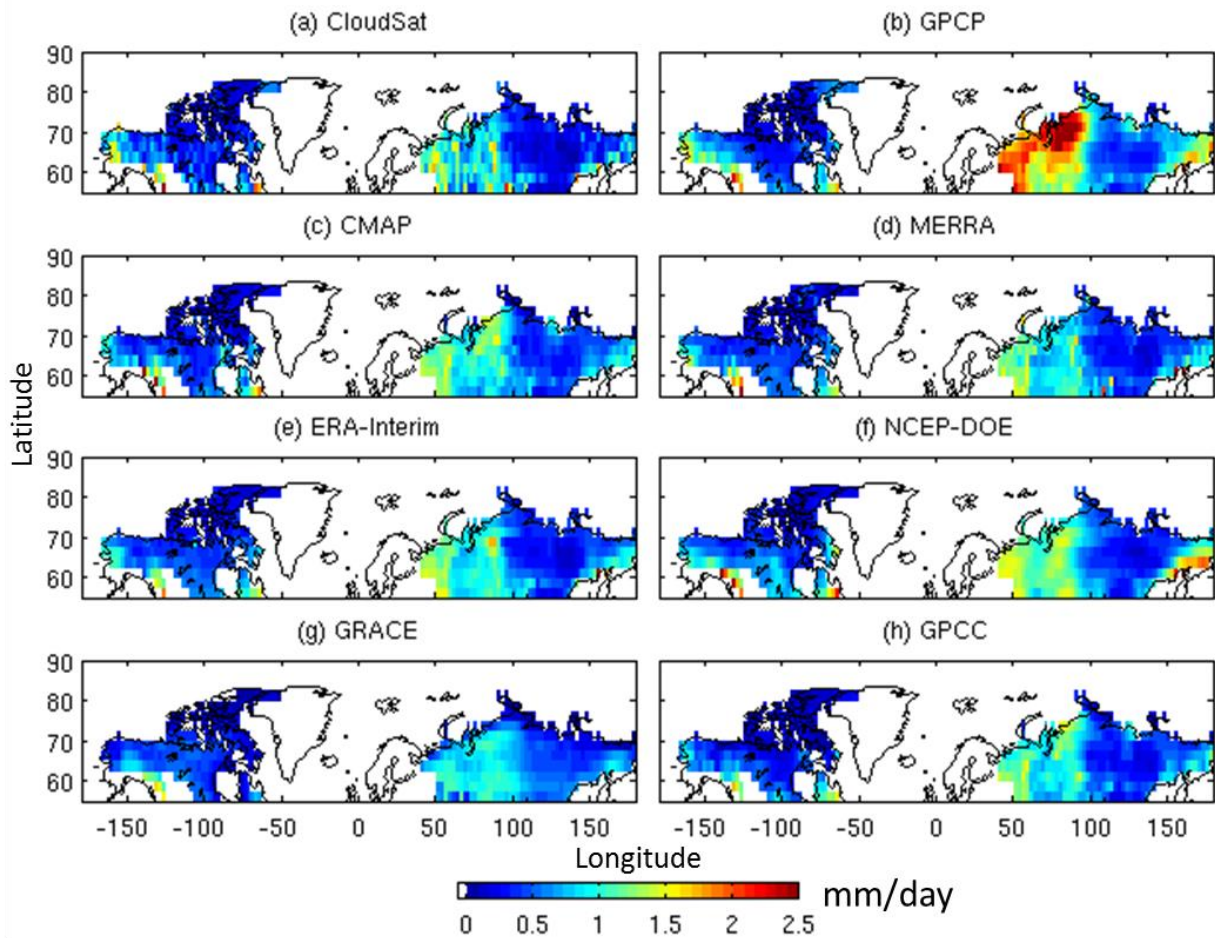


Figure 7. Comparison of wintertime estimate of snowfall rate from GRACE (Fig 6g) with the other products. Only grids experiencing mean 2m air temperatures below  $-1^{\circ}\text{C}$  across all days in boreal winter are considered for this comparison.

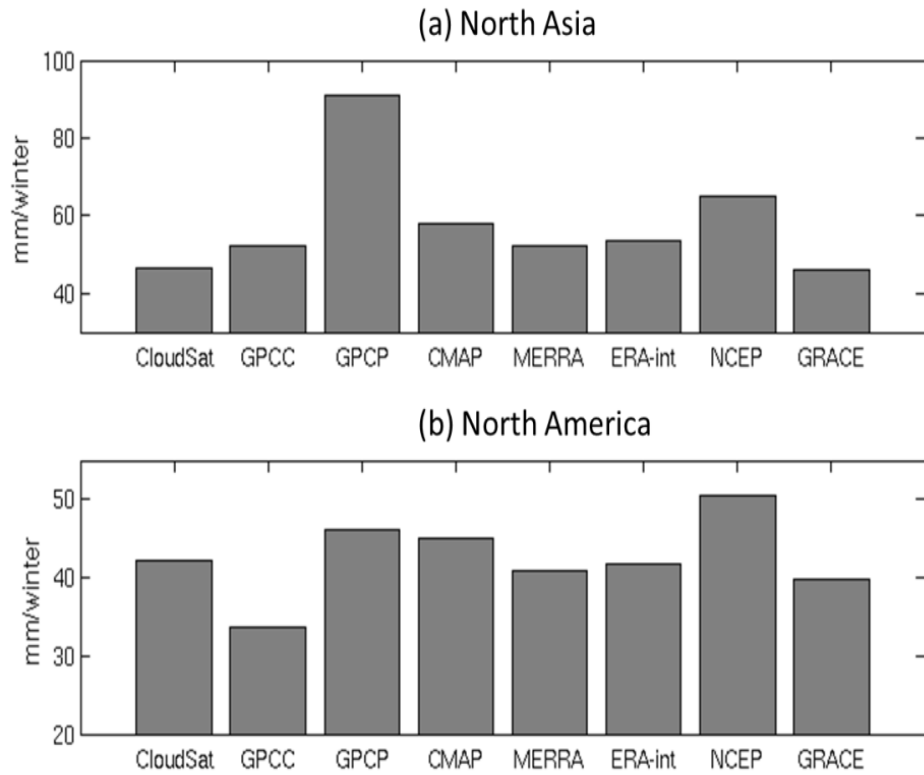


Figure 8. Comparison between 2007-2010 mean accumulated boreal winter snowfall estimated by different products separately over (a) Northern Asia and (b) Northern America. The two regions are identical to those shown in Figure 6.

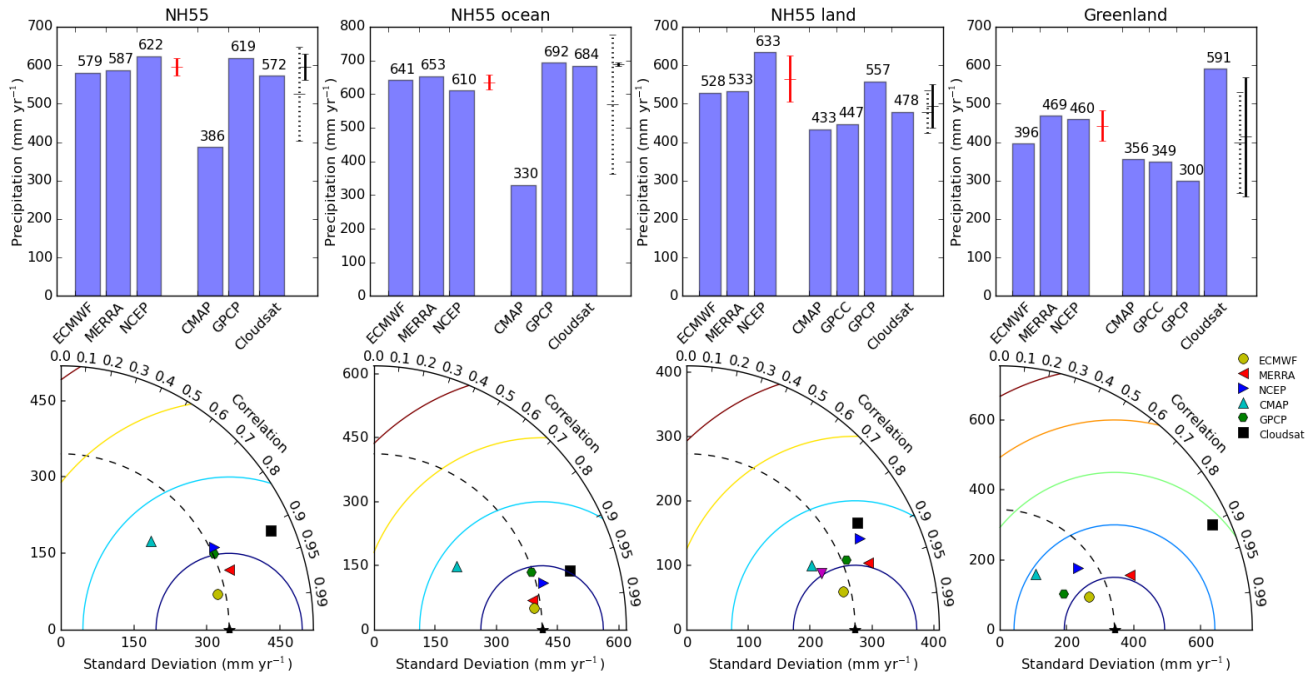


Figure 9: Precipitation statistics for each product by region. Top row: bar charts show mean precipitation (2007-2010) within region by product, organized as reanalyses (left 3 bars) and observations (right bars). The red solid bar shows the mean  $\pm 1$  standard deviation of the reanalysis product means, the dashed black bar shows the mean  $\pm 1$  standard deviation of the observational series GPCP, CMAP and CloudSat, and the solid black bar is the same excluding CMAP. Bottom row: Taylor diagrams of the same regions, product symbols shown in legend (far right) and the reference (black star) is the mean of the reanalyses plus the geographically complete observations GPCP and CloudSat. Regions are, from left to right: the entire NH (55-80°N), NH oceans (55-80°N), NH land (55-80°N), and Greenland.

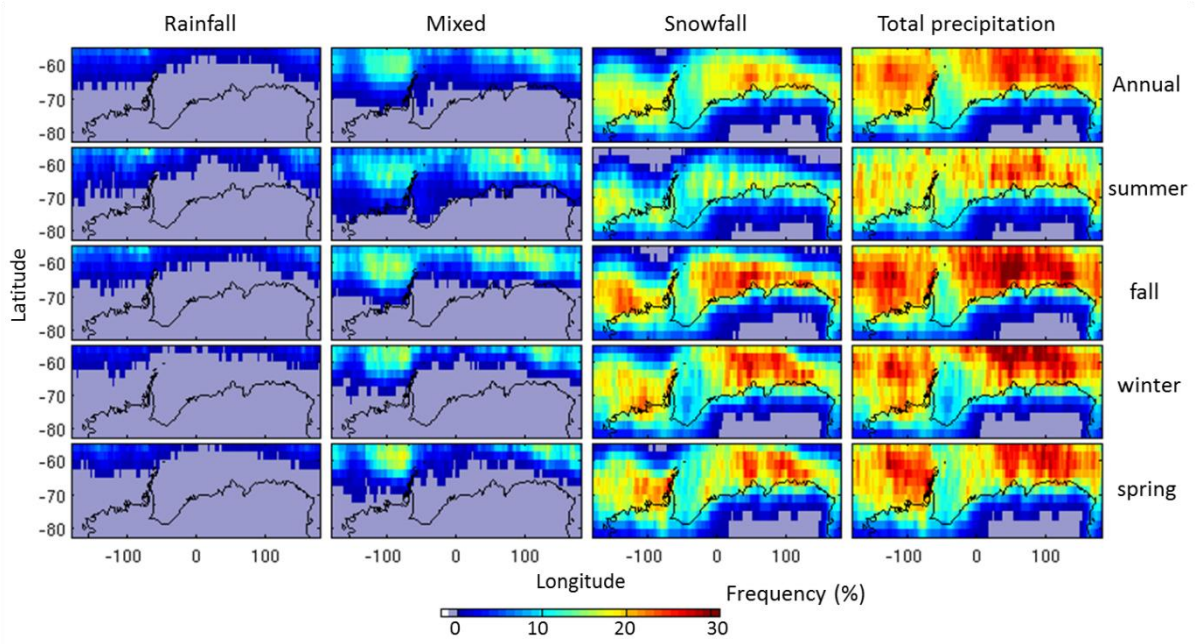


Figure 10. Maps of annual and seasonal rain, snow, and precipitation frequencies from CloudSat observations for 2007-2010. The first row displays the annual frequencies and the remaining rows are for precipitation frequencies for each of the four austral seasons: summer (DJF), fall (MAM), winter (JJA), and spring (OND).

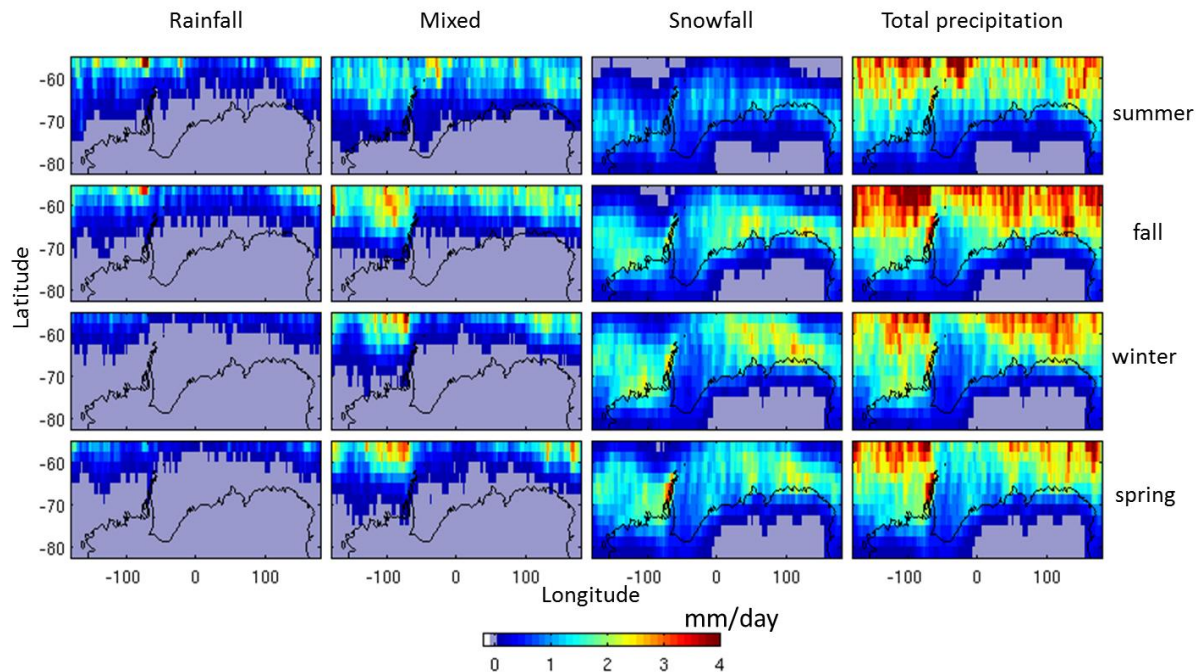


Figure 11. Maps of seasonal precipitation rates from CloudSat for 2007-2010, stratified by precipitation phases. From left to right columns represent mean rainfall, mixed-phase, snowfall, and total precipitation and rows display the four austral seasons.

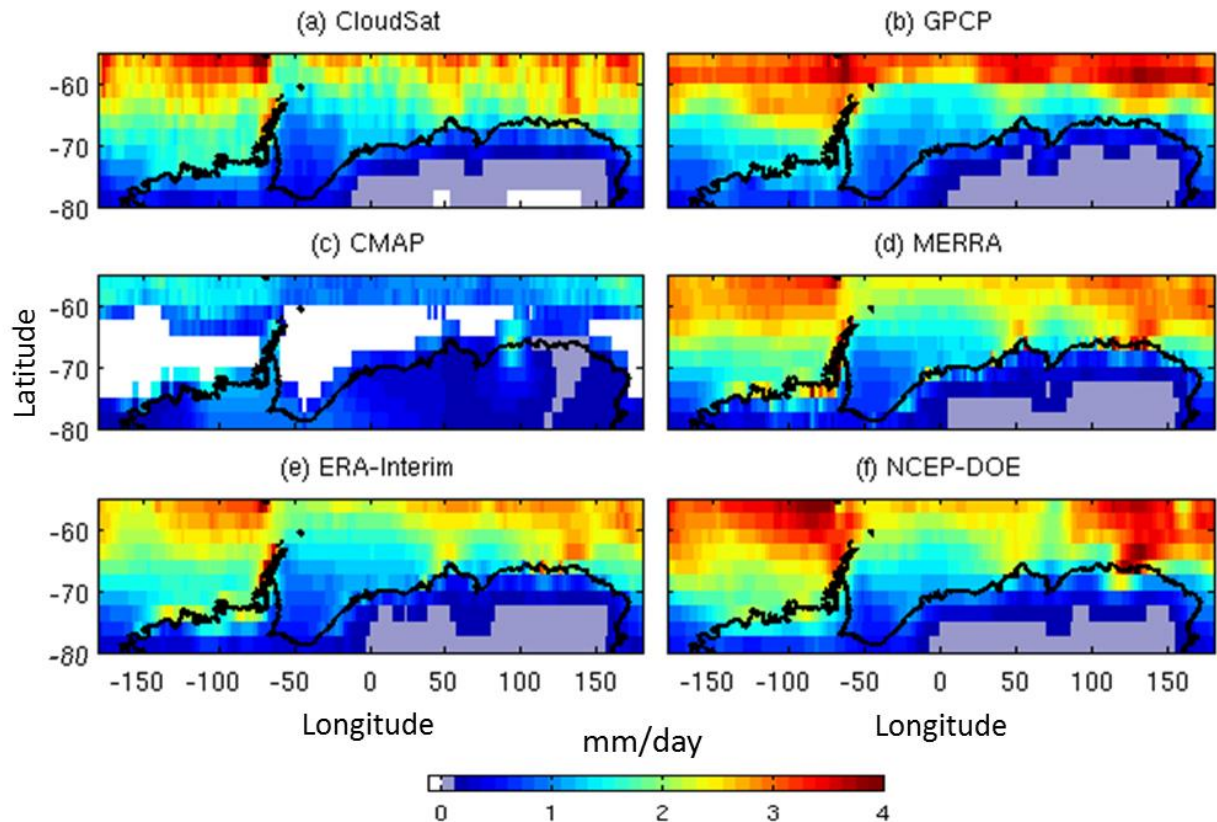


Figure 12. Maps of 2007-2010 averaged precipitation rates (mm/day) constructed from CloudSat, GPCC, GPCP, CMAP, MERRA, ERA-interim, NCEP, and GLDAS over land and ocean south of latitude 55°. White areas represent missing or non-reported data.

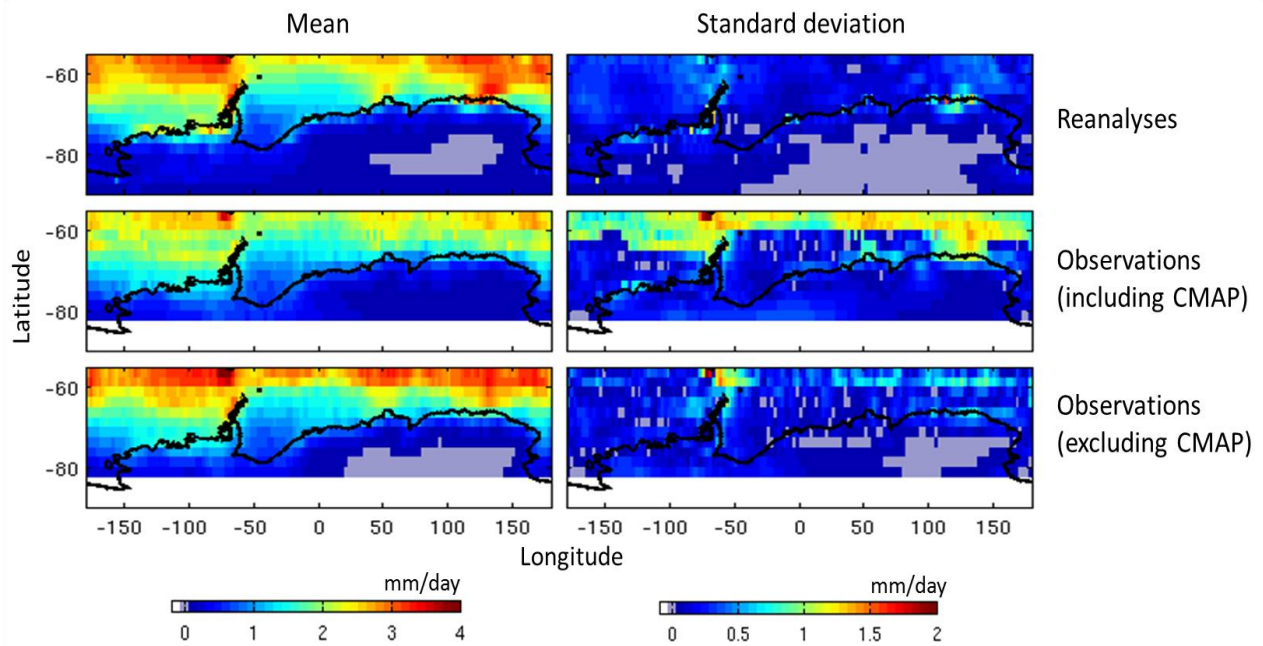


Figure 13. Maps of mean and standard of precipitation estimates, calculated separately for reanalysis (MERRA, ERA-Interim, NCEP; bottom row) and observation (GPCP, CMAP, CloudSat) products in SH for 2007-2010.

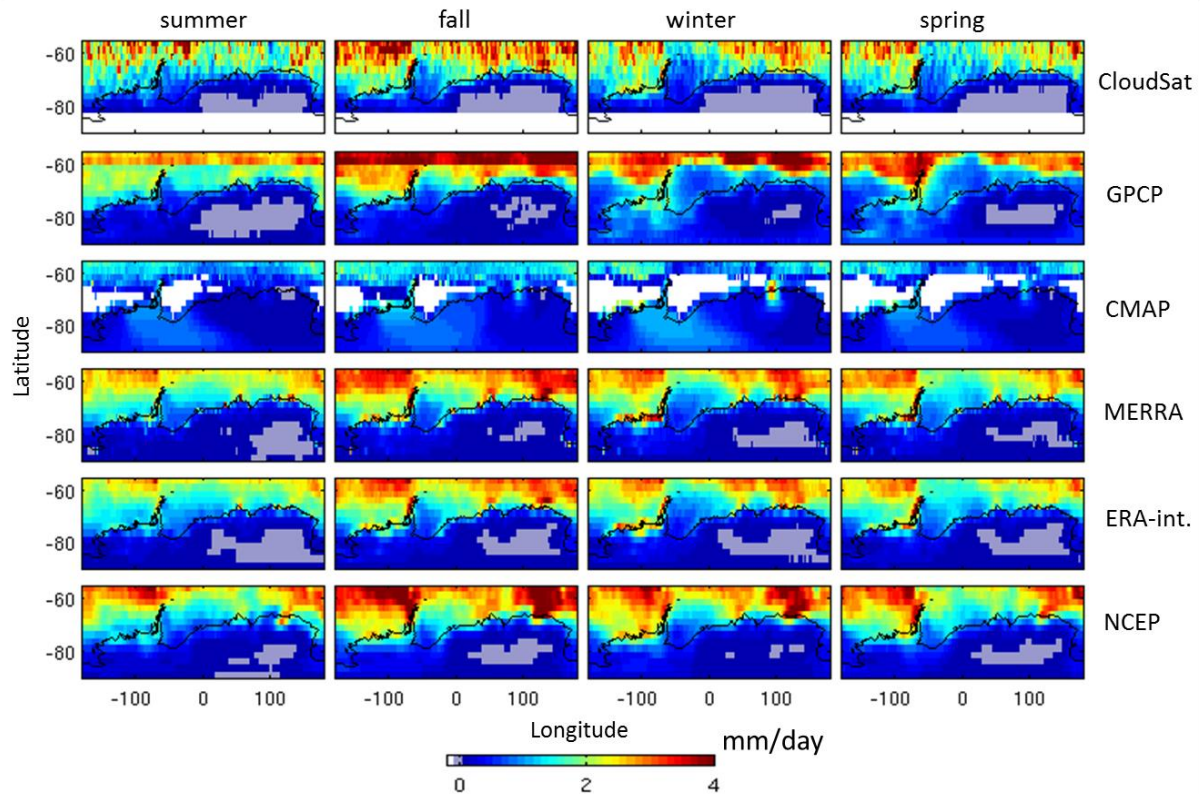


Figure 14. Maps of precipitation mean intensity for the studied products (shown in rows) across the four austral seasons in SH for 2007-2010. White areas represent missing or non-reported data.

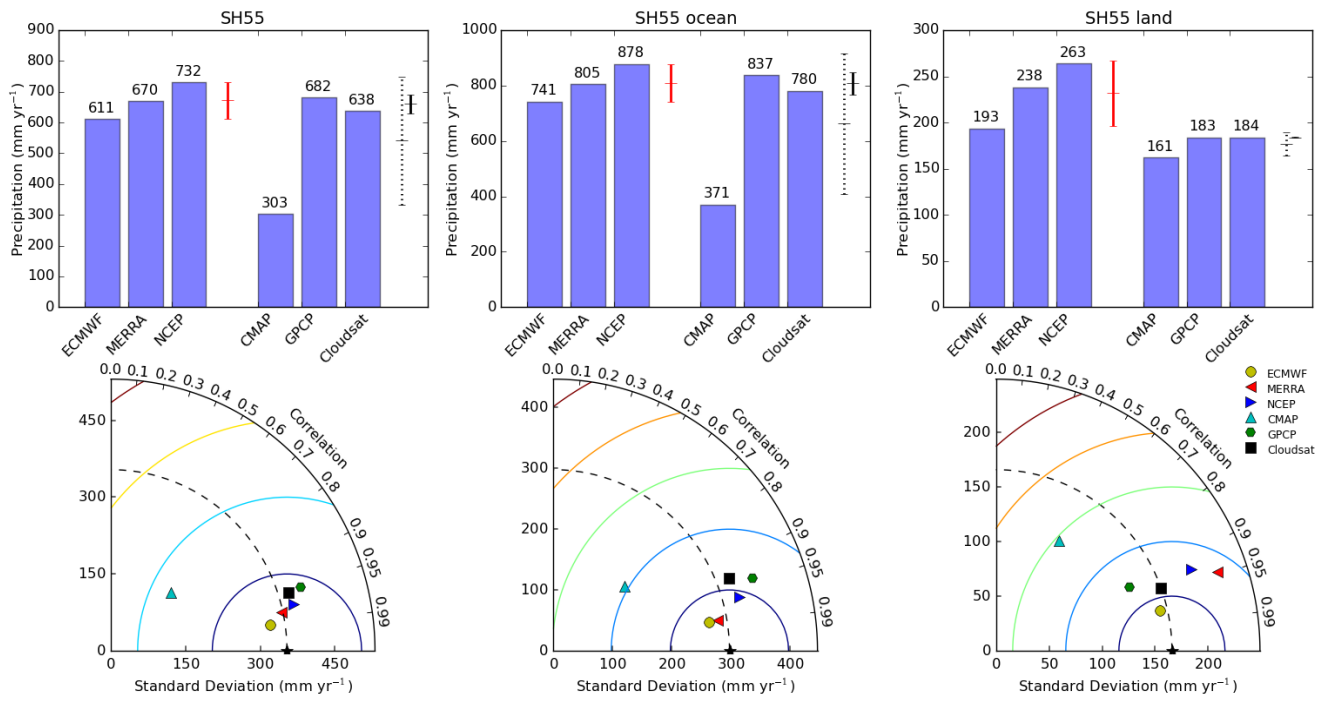


Figure 15. Similar to Fig. 9, but for Southern Hemisphere 55-80° (SH55). Regions are, from left to right: the entire SH (55-80°S), SH oceans (55-80°S), and SH land (55-80°S)(Antarctica). GPCC has no data over Antarctica and is not shown.